

Limits on the atmospheric metallicity and aerosols of the sub-Neptune GJ 3090 b from high-resolution CRIRES+ spectroscopy

Luke T. Parker[®], ^{1★} João M. Mendonça[®], ^{2,3,4} Hannah Diamond-Lowe, ^{2,5} Jayne L. Birkby [®], ¹ Annabella Meech [®], ⁶ Sophia R. Vaughan [®], ^{1,7} Matteo Brogi, ^{8,9} Chloe Fisher [®], ¹ Lars A. Buchhave [®], ² Aaron Bello-Arufe, ^{2,10} Laura Kreidberg and Jason Dittmann ^{7,11}

Accepted 2025 March 19. Received 2025 March 10; in original form 2025 January 10

ABSTRACT

The sub-Neptune planets have no solar system analogues, and their low bulk densities suggest thick atmospheres containing degenerate quantities of volatiles and H/He, surrounding cores of unknown sizes. Measurements of their atmospheric composition can help break these degeneracies, but many previous studies at low spectral resolution have largely been hindered by clouds or hazes, returning muted spectra. Here, we present the first comprehensive study of a short-period sub-Neptune using ground-based, high-resolution spectroscopy, which is sensitive to the cores of spectral lines that can extend above potential high altitude aerosol layers. We observe four CRIRES+ K-band transits of the warm sub-Neptune GJ 3090 b ($T_{eq} = 693\pm18$ K) which orbits an M2V host star. Despite the high quality data and sensitivity to CH₄, H₂O, NH₃, and H₂S, we detect no molecular species. Injection-recovery tests are consistent with two degenerate scenarios. First, GJ 3090 b may host a highly metal-enriched atmosphere with > 150 Z_{\odot} and mean molecular weight > 7.1 g mol⁻¹, representing a volatile dominated envelope with a H/He mass fraction $x_{\rm H/He} < 33$ per cent, and an unconstrained aerosol layer. Second, the data are consistent with a high altitude cloud or haze layer at pressures $< 3.3 \times 10^{-5}$ bar, for any metallicity. GJ 3090 b joins the growing evidence to suggest that high metallicity atmospheres and high altitude aerosol layers are common within the warm ($500 < T_{\rm eq} < 800$ K) sub-Neptune population. We discuss the observational challenges posed by the M-dwarf host star, and suggest observing strategies for transmission spectroscopy of challenging targets around M-dwarfs for existing and ELT instrumentation.

Key words: techniques: spectroscopic – planets and satellites: atmospheres – planets and satellites: individual: GJ 3090 b.

1 INTRODUCTION

The prevalence of small exoplanets on orbits of less than 10 days is one of the most unexpected discoveries in the detection of planets beyond our Solar System (Batalha 2014). Population studies have revealed that these small close-in exoplanets are divided into two distinct categories: the super-Earths ($R_p \lesssim 1.7 \, R_{\bigoplus}$) and sub-Neptunes (1.7 $R_{\bigoplus} \lesssim R_p \lesssim 4 \, R_{\bigoplus}$; e.g. Rogers 2015; Fulton et al. 2017; Fulton & Petigura 2018; Van Eylen et al. 2018; Dattilo & Batalha 2024). The terrestrial super-Earths have bulk densities similar to

that of Earth and Venus, but sub-Neptunes have no Solar System analogues. Their low bulk densities point to thick atmospheres containing substantial quantities of hydrogen and helium alongside water and volatiles, surrounding degenerate amounts of iron and silicates in solid cores of unknown sizes (Rogers & Seager 2010; Dorn et al. 2017; Hu et al. 2021; Yu et al. 2021; Luque & Pallé 2022). This compositional uncertainty has led to the proposition of a range of possible planetary structures including H/He dominated, low mean molecular weight atmospheres ('Gas Dwarf'; e.g. Fortney et al. 2013; Buchhave et al. 2014; Lopez & Fortney 2014); high metallicity envelopes composed of miscible H/He and metals ('Miscible Envelope sub-Neptune'; Benneke et al. 2024); H₂O dominated, high mean molecular weight atmospheres ('Water

¹Department of Astrophysics, University of Oxford, Denys Wilkinson Building, Keble Road, Oxford OX1 3RH, UK

²Department of Space Research and Space Technology, Technical University of Denmark, Elektrovej 328, DK-2800 Kgs. Lyngby, Denmark

³School of Physics and Astronomy, University of Southampton, Highfield, Southampton SO17 1BJ, UK

⁴School of Ocean and Earth Science, University of Southampton, Southampton SO14 3ZH, UK

⁵Space Telescope Science Institute, 3700 San Martin Drive, Baltimore, MD 21218, USA

⁶Center for Astrophysics, Harvard and Smithsonian, 60 Garden Street, Cambridge, MA 02138, USA

⁷Max-Planck-Institut fur Astronomie, Konigstuhl 17, D-69117 Heidelberg, Germany

⁸Dipartimento di Fisica, Università degli Studi di Torino, via Pietro Giuria 1, I-10125 Torino, Italy

⁹INAF – Osservatorio Astrofisico di Torino, Via Osservatorio 20, I-10025 Pino Torinese, Italy

¹⁰Jet Propulsion Laboratory, California Institute of Technology, Pasadena, CA 91109, USA

¹¹Department of Astronomy, University of Florida, Gainesville, FL 32611, USA

^{*} E-mail: luke.parker@physics.ox.ac.uk

Worlds'; e.g. Mousis et al. 2020; Aguichine et al. 2021; Piaulet et al. 2023; Pierrehumbert 2023; Piaulet-Ghorayeb et al. 2024); and H/He dominated atmospheres with a defined surface–atmosphere boundary, either a transition to a liquid water ocean ('Hycean worlds'; e.g. Hu et al. 2021; Madhusudhan, Piette & Constantinou 2021; Madhusudhan et al. 2023), or a magma ocean (e.g. Kite et al. 2020; Schlichting & Young 2022; Zilinskas et al. 2023; Shorttle et al. 2024). These scenarios, which are degenerate when considering only the bulk planetary parameters, can be broken through atmospheric observations (Bean, Raymond & Owen 2021). Constraints on the mean atmospheric weight can provide boundary conditions for models of interior structure (Dorn et al. 2017; Nixon & Madhusudhan 2021), while the measurement of atmospheric composition can probe surface-atmosphere exchange (Misener, Schlichting & Young 2023; Shorttle et al. 2024). Specifically, measurements of the atmospheric metallicity (Nixon et al. 2024), C/O ratio (Seo, Ito & Fujii 2024), mean molecular weight (Benneke et al. 2024), and the abundances of individual atmospheric constituents (Madhusudhan et al. 2023; Shorttle et al. 2024; Yang & Hu 2024), have all been suggested to distinguish between the large range of scenarios proposed.

H/He-rich atmospheres are predicted to produce large signals of trace species in transmission spectra due to their large-scale heights, and sub-Neptunes have been targeted extensively at low resolution with HST/WFC3's G141 grism (e.g. Kreidberg et al. 2014; Benneke et al. 2019; Guo et al. 2020; Mikal-Evans et al. 2021, 2023; Roy et al. 2023). However, observations have predominantly returned flat or muted spectra relative to what is predicted for a clear atmosphere, suggesting high-altitude clouds or hazes (collectively aerosols) that obscure the targeted molecular features (e.g. Kreidberg et al. 2014). Initial population studies have suggested that these aerosol abundances, and consequently the strength of the attenuation, follow trends with equilibrium temperature, but are prevalent across a large temperature range (300 $< T_{eq} < 900 \text{ K}$; Morley et al. 2015; Crossfield & Kreidberg 2017; Brande et al. 2024). The study of these enigmatic worlds at low-resolution has been transformed by the advent of precise near-infrared spectroscopy with JWST, with molecular detections of CH₄, CO₂, H₂O in cool and warm sub-Neptunes (e.g. Madhusudhan et al. 2023; Benneke et al. 2024; Holmberg & Madhusudhan 2024; Piaulet-Ghorayeb et al. 2024; Davenport et al. 2025), but the obscuration of spectral features in transmission by aerosols remains a fundamental limitation of many observations at low spectral-resolution (e.g. GJ 1214 b; Kempton et al. 2023; Ohno et al. 2025; Schlawin et al. 2024).

However, observations using ground-based high-resolution crosscorrelation spectroscopy at $R \approx 100\,000$ (HRCCS; see Birkby 2018) are additionally sensitive to the cores of spectral lines that extend above the aerosol layer and are therefore predicted to be sensitive to the unique spectral lines of molecules in sub-Neptune atmospheres, even in the presence of a high altitude aerosols (de Kok et al. 2014; Kempton, Perna & Heng 2014; Pino et al. 2018; Gandhi, Brogi & Webb 2020; Hood et al. 2020). This detectability relies upon the assumption of well-mixed atmospheres, such that targeted molecules are present in sufficient abundances above the cloud deck to form strong spectral lines. Shallow atmospheres and the presence of a surface have been proposed to inhibit thermochemical kinetics and mixing on sub-Neptunes, leading to the depletion of nitrogen-based species (e.g. NH₃, HCN) in the presence of shallow surfaces ($\lesssim 10$ bar; Yu et al. 2021), but the abundances of key molecules including CH₄, CO and H₂O are largely invariant to this effect (Hu et al. 2021; Yu et al. 2021).

While transmission spectroscopy with HRCCS has proved highly successful in characterizing the population of Jupiter mass planets

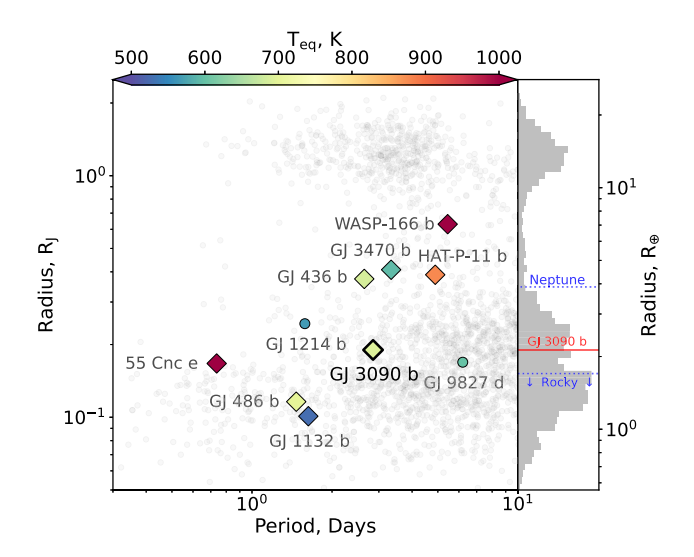


Figure 1. The sub-Neptune GJ 3090 b compared to the small population of short period, sub-Jovian planets studied with HRCCS (diamonds). Of the planets shown only HAT-P-11 b has produced confirmed molecular detections using HRCCS, while all other HRCCS studies have placed upper limits. The feasibility of HRCCS to explore the enigmatic sub-Neptune regime (with radii less than Neptune) remains largely untested. GJ 1214 b and GJ 9827 d, which have been studied in detail at low spectral resolution, are highlighted for comparison.

(e.g. Snellen et al. 2010; Brogi et al. 2016; Hoeijmakers et al. 2018a; Prinoth et al. 2022; Pelletier et al. 2023; Nortmann et al. 2025), it is only beginning to push to smaller targets. In the Neptune/Saturn mass regime, Lafarga et al. (2023), Dash et al. (2024), and Grasser et al. (2024) observed WASP-166 b, GJ 3470 b, and GJ 436 b, respectively and, while they are unable to detect molecular species in the planetary atmospheres, place constraints on their metallicities and the altitude of cloud decks. Basilicata et al. (2024) report the detection of NH₃ and H₂O in the warm, Neptune-mass, HAT-P-11 b using GIANO-B, the smallest planet in which molecular detections have been found using HRCCS to date (see Fig. 1). Attempts have also been made to observe rocky worlds with HRCCS, with efforts focused on 55 Cancri e, none of which have detected atmospheric features (Ridden-Harper et al. 2016; Esteves et al. 2017; Jindal et al. 2020; Deibert et al. 2021; Keles et al. 2022), while some clear H/He dominated atmosphere scenarios have also been ruled out for GJ 486 b (Ridden-Harper et al. 2023) and GJ 1132 b (Palle et al. 2025).

The sub-Neptune regime however, in which we anticipate a diverse range of atmospheric compositions, remains unexplored, with no reported studies of sub-Neptunes on short orbits that are readily accessible by traditional HRCCS. The only existing work on a sub-Neptune using HRCCS revolves around a single transit of TOI-732 c with IGRINS/Gemini-S (Cabot et al. 2024), attempting to extend the viability of the HRCCS technique to longer period, temperate exoplanets. The scarcity of observations is, in part, a result of the novel challenges to HRCCS observations presented by sub-Neptunes, foremost the small spectral features in transmission which necessitate bright host stars with favourable star–planet radius ratios. The most favourable sub-Neptune targets for atmospheric characterization therefore orbit bright M-dwarf host stars, producing additional observational challenges due to their activity and spectroscopic features (see Section 5.2). Recent advances in instrumentation, most notably the recent upgrade to CRIRES/VLT (Dorn et al. 2014, 2023),

Table 1. The stellar and planetary parameters of the GJ 3090 b system. A22: Almenara et al. (2022), G21: Gaia Collaboration (2021), C03: Cutri et al. (2003).

Parameter	Value	Reference	
	GJ 3090: stellar parameters		
RA	01 ^h 21 ^m 45 ^s .390170	G21	
Dec	$-46^{\circ}42'51.76497$ arcsec	G21	
K	$7.29\pm0.03~{\rm mag}$	C03	
R⋆	$0.516\pm0.016~R_{\odot}$	A22	
M_{\star}	$0.519\pm0.013~{\rm M}_{\odot}$	A22	
T_{eff}	3556±70 K	A22	
Spectral type	M2V	A22	
[Fe / H]	-0.060 ± 0.120	A22	
vsin(i)	$< 1.47 \pm 0.05 \text{ km s}^{-1}$	A22	
Distance	$22.444\pm0.013 \text{ pc}$	A22	
$v_{ m sys}$	$17.4095 \pm 0.0046 \; \mathrm{km} \; \mathrm{s}^{-1}$	A22	
	GJ 3090 b: planetary parameters		
T_{eq}	693±18 K	A22	
Rp	$2.13{\pm}0.11~R_{\oplus}$	A22	
$\dot{M_p}$	$3.34{\pm}0.72~{ m M}_{\oplus}$	A22	
$ ho_{ m p}$	$1.89^{+0.52}_{-0.45} \text{ g cm}^{-3}$	A22	
Porb	2.8531054 ± 0.0000023 days	A22	

offers the first practical opportunity to observe the atmospheres of these enigmatic sub-Neptunes at high spectral resolution.

In this work we observe four transits of GJ 3090 b, a $M_p = 3.34 \pm$ $0.72M_{\bigoplus}$, $R_p = 2.13 \pm 0.11R_{\bigoplus}$ sub-Neptune around a bright (K =7.3 mag) M2V dwarf (Almenara et al. 2022), see Table 1. Its low density of $\rho_p=1.89^{+0.52}_{-0.45}$ g cm⁻³ appears consistent with a primordial H/He envelope, while the location of GJ 3090 b immediately above the radius valley (Fulton et al. 2017), places it in an ideal region of the parameter space to probe the transition between super-Earths and sub-Neptunes (Bean et al. 2021; Parc et al. 2024). GJ 3090 b has an equilibrium temperature of $T_{\rm eq} = 693 \pm 18$ K, and is predicted to be among the most readily observable sub-Neptunes for transmission spectroscopy with a transmission spectroscopy metric (TSM; Kempton et al. 2018) of 221+66, second only to GJ 1214 b (Almenara et al. 2022), under the assumption of a clear H/He dominated atmosphere. While the TSM was developed for low resolution JWST/NIRISS observations and normalized to the J-band magnitude, it encapsulates both the predicted atmospheric scale height and the brightness of the host star in the NIR, making it a reasonable metric to also apply to K-band HRCCS transmission observations.

With a total of 10 h of observations, targeting the optimal spectral regions in the *K*-band, we carry out the first comprehensive study of a sub-Neptune using ground-based HRCCS. We detail our CRIRES+ observations in Section 2. Section 3 discusses our data processing, modelling, and analysis procedure, with results and injection tests presented in Section 4. In Section 5 we discuss the constraints on the atmosphere of GJ 3090 b, and their implications for future studies, alongside recommended observing strategies for existing and future instrumentation. We conclude in Section 6.

2 OBSERVATIONS

We observed four transits of GJ 3090 b with the upgraded Cryogenic High-Resolution In-frared Echelle Spectrograph (CRIRES+; Dorn et al. 2014, 2023), mounted at the Nasmyth B focus of the VLT UT3 (Melipal). Our observations, totalling 10 h of observing time over the four transits (see Table 2), were taken between 2022 August

Table 2. Details of the 1.92–2.47 μm K2166 CRIRES+ observations of GJ 3090 b.

	Transit 1	Transit 2	Transit 3	Transit 4
UTC Date	08/08/2022	07/10/2022	27/10/2022	30/10/2022
Avg. PWV	2.26 mm	1.65 mm	0.38 mm	0.64 mm
Avg. Seeing	0.56 arcsec	0.47 arcsec	0.46 arcsec	0.62 arcsec
Avg. Airmass	1.11	1.12	1.18	1.17
$N_{\rm exp}$	54	50	48	46
DIT	180 s	180 s	180 s	180 s
Slit Width	0.2 arcsec	0.2 arcsec	0.2 arcsec	0.2 arcsec
Resolution	148 000	140 000	153 000	144 000
v_{bary} at T_0	$11.68 \; \mathrm{km} \mathrm{s}^{-1}$	$-6.92 \; \mathrm{km} \mathrm{s}^{-1}$	$-12.72~{\rm kms^{-1}}$	$-13.19 \mathrm{km} \mathrm{s}^{-1}$

8 and October 30 (Programme ID: 109.232F, PI: Diamond-Lowe). Each transit had a duration $T_{14} = 1.281 \pm 0.024$ h (Almenara et al. 2022), and an additional out of transit baseline of $\approx T_{14}$ was observed per transit. The propagated uncertainty on the transit time of 25 s yr⁻¹ leads to a transit midpoint that is constrained to a precision of ± 100 s, less than the duration of a single 180 s exposure with CRIRES+. The upgraded CRIRES operates as a cross-dispersed slit spectrograph and the slit width of 0.2 arcsec was chosen to achieve the maximum spectral resolving power offered by CRIRES+, nominally $R \sim 92\,000$ when the resolution is limited by the slit width. The Multi-Application Curvature Adaptive Optics system (MACAO; Paufique et al. 2004) system is used with GJ 3090 as the AO natural guide star. The use of MACAO provides both an enhanced S/N and, in good observing conditions, a spectral resolution $R \gg 92\,000$, limited by the PSF width. We observed in the K2166 grating setting, which provides discontinuous wavelength coverage across the range 1.92-2.47 um over seven orders. The K-band provides sensitivity to key atmospheric species predicted to be found in warm sub-Neptunes including H₂O, CH₄, CO, CO₂, NH₃, and H₂S. Furthermore, the Mdwarf host is bright at K-band wavelengths (K = 7.3 mag), and the spectra remain relatively unaffected by thermal background noise compared to observations at longer wavelengths (e.g. Parker et al. 2024). The K2166 grating is specifically chosen as it provides a good coverage of target spectral features and has a shallow blaze function, ensuring high S/N spectra across each spectral order. Exposures were taken in the classical ABBA nod pattern (NDIT=1, NEXP=1), during which the telescope was nodded 6 arcsec along the slit, to allow accurate background subtraction. Transits were selected for the optimum airmass and achieve excellent observing conditions, with an average airmass of 1.15 and an average DIMM measured seeing of 0.53 arcsec across the four transits.

2.1 Archival data: two CRIRES+ K2148 transits

We additionally analyse two archival CRIRES+ transits of GJ 3090 b taken using the K2148 grating. These transits total an additional 5.5 h of observing time, observed on the nights of 2023 August 11 and September 3 (Programme ID: 0111.C-0106 GTO, PI: Nortmann). The CRIRES+ slit width of 0.2 arcsec and MACAO were used and exposures were taken in the classical ABBA nod pattern (NDIT=1, NEXP = 1). The use of the K2148 grating setting, which partially overlaps with the K2166 setting used in the primary data set, provides discontinuous wavelength coverage across the range 1.97–2.45 µm over six usable orders. However, in comparison to the excellent observing conditions achieved over the four K2166 transits which form the primary data set in this work (see Fig. 2), the additional transits are taken in more challenging conditions. The average seeing was highly variable across both transits, with an average

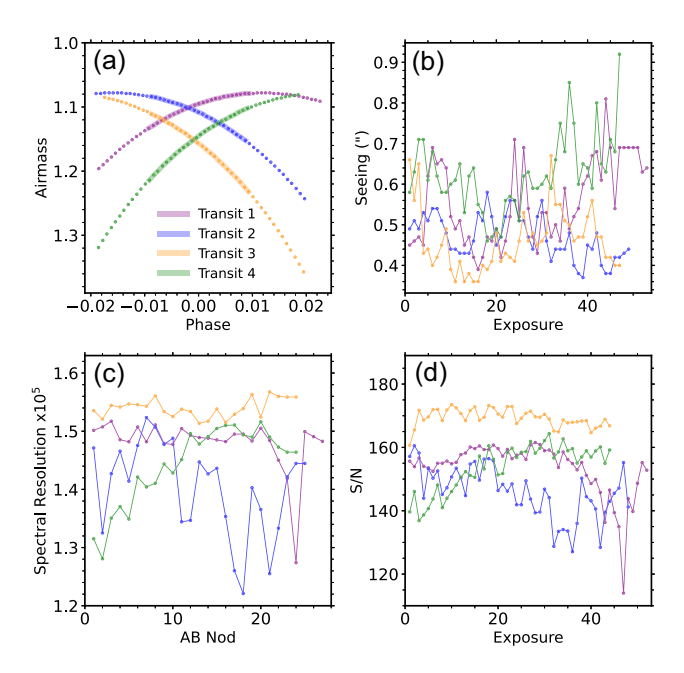


Figure 2. The observing conditions for the four CRIRES+ K2166 transits analysed in this work. (A) airmass of each observed transit, optimized to occur near zenith. (B) seeing conditions over the course of each transit, as measured by DIMM sensors at the observatory, which remain largely stable per night. (C) measured spectral resolution of the exposures in each AB nodding pair. Due to the excellent observing conditions and MACAO performance, this is controlled by the PSF width, and is thus far in excess of the nominal slit width limited resolution of CRIRES+, $R \sim 92\,000$. (D) average S/N per spectral bin for each exposure.

of 0.81 and 1.10 arcsec for the two K2148 transits, respectively, while the radiometer measured precipitable water vapour (PWV) for both transits is variable over the night, reaching maxima of 2.8 and 4.31 ppm. The inclusion of these additional transits therefore do not appreciably improve the strength of our constraints on the atmosphere of GJ 3090 b. None the less, we examine the limitations of these data in comparison to the highly constraining K2166 transits, and discuss the lessons learned for future observations of sub-Neptunes with HRCCS in Section 4.2 and Section 5.2.

3 METHODS

3.1 Basic calibrations

Basic calibrations are carried out using PYCRIRES¹ (Stolker & Landman 2023; Landman et al. 2024), an open source python wrapper for the ESOREX cr2res routines². The raw frames are flat-fielded and dark subtracted to remove detector and readout artefacts present in the raw exposures. Detector non-linearity corrections are applied, bad pixels are flagged, and the imprinted blaze function is corrected. Each exposure (A or B) is subsequently subtracted from its corresponding nodding pair (B or A), providing an effective background subtraction as the spectral trace at the A and B nodding positions fall on different regions of the detector. From each background-subtracted exposure a 1D science spectrum of the star is optimally extracted at both the A and B nod positions for each spectral order (Horne

1986), considering the slit-image curvature, which in the K-band is accurately calibrated using the Fabry-Pérot Etalon (FPE) System (Dorn et al. 2023). In the K2166 grating setting, seven spectral orders are dispersed across the CRIRES+ detector focal plane array, consisting of three adjacent Hawaii 2RG detectors, each with dimensions of 2048×2048 pixels. Further details of the initial spectral extraction can be found in Appendix A. Due to the excellent performance of the CRIRES+ MACAO system, the stellar point spread function (PSF) is sufficiently narrow that it does not evenly fill the 0.2 arcsec slit. The PSF is measured to have an average fullwidth half-maximum (FWHM) of ≈ 2.2 pixels in the spatial direction of the CRIRES+ detectors, where a FWHM of 3.6 pixels would correspond to the width of the 0.2 arcsec slit. This effect, known as super-resolution, produces observations with a spectral resolution determined by the PSF width, rather than the slit width, resulting in a much higher than average resolving power of R = 146000across the four transits. The resolving power is measured from the observed PSF width in the spatial direction following Nortmann et al. (2025).

Due to the narrow AO-assisted PSF, the PSF centre can shift within the slit over the course of the observations. If we assume that the motion of the PSF is stochastic, we can use the vertical shift of the PSF within the slit as a proxy for the shift across the slit width. We measure an average standard deviation in the vertical placement of the PSF of 0.00672 arcsec, which would correspond to shifts of 3 per cent of the slit width. Despite the stability of the PSF core in the slit this can result in shifts on the detector on the order of a few pixels between spectra extracted from the A and B nodding positions for each transit. This effect is independent of the offset of spectra from A and B nods which arises from the misalignment of the CRIRES+ slit tilt with respect to the detector columns, which is accounted for in the wavelength calibration. Furthermore, the narrow FWHM of the stellar signal results in enhanced contamination from individual bad pixels that intersect the trace at either nod position, leading to discrepant systematic effects at the pixel level for the spectra extracted from the A or B nod positions. In order to limit the impact of these offsets and nod-dependent systematic effects, spectra at the A and B nod positions are subsequently reduced independently, and only combined following cross-correlation.

All spectra from each nodding position are aligned to a common wavelength grid for the nod and ordered in phase, with the grids of both the A and B spectra maintaining the original detector pixel scale. Initial wavelength calibration of the spectra is carried out using the UNe lamp as the stable wavelength reference source, with additional corrections applied by the FPE. Finally, to ensure an accurate wavelength calibration a telluric model from MOLECFIT (Smette et al. 2015) is used as the stable reference source, and cross-correlated with the second spectrum of each night to produce a refined wavelength solution for each nodding position.

An alternative solution to the CRIRES+ AB nod offsets is to align all the extracted spectra from both nodding positions onto a common wavelength grid (e.g. Nortmann et al. 2025). We additionally test this method, aligning the A and B nods from each nodding pair by cross-correlating each AB nod pair with each other, then aligning to a common wavelength grid. While this approach produced excellent alignment between the spectra, the combination of nod-specific systematics from the A and B nods adversely affected the cleaning process, resulting in a marginally lower detection significance when carrying out injection recovery tests. As this method requires additional interpolation of the primary data products, we therefore reduce the extracted spectra from the A and B nod positions independently.

¹https://pypi.org/project/pycrires/

²https://www.eso.org/sci/software/pipe_aem_table.html

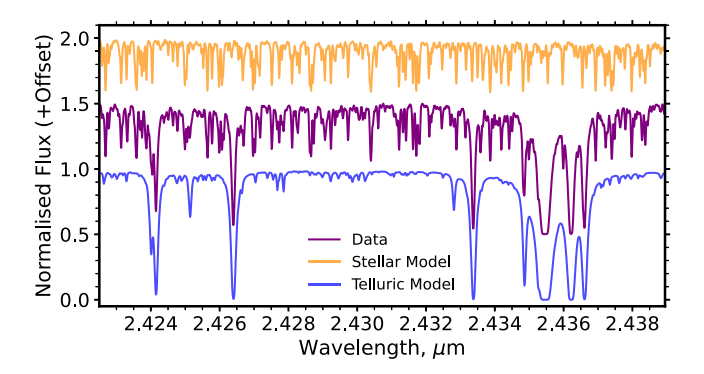


Figure 3. The stellar (orange) and telluric (blue) contributions to the observed CRIRES+ spectra of GJ 3090 (purple). Note the near universal wavelength coverage of stellar lines, rendering established analysis techniques such as masking stellar lines unfeasible, and the simultaneous modelling of telluric and stellar spectra highly challenging.

3.2 Post-processing

At this stage in the reduction process the dominant features in the spectra are telluric absorption features and stellar lines from the M-Dwarf host star GJ 3090 (see Fig. 3). Each of these components is stationary with time within its own reference frame, and we choose to perform our cleaning procedure in the stellar rest frame, which successfully removes contamination from the M-dwarf host, without significantly compromising the removal of telluric features (Nortmann et al. 2025). The stellar features are ubiquitous across the wavelength range observed, and residuals from their imperfect correction have the largest impact in cross-correlation space (see Section 5.2.1), as they overlap with the systemic velocity of potential planetary signals, and we therefore prioritize their correction when removing systematics from the data.

Our cleaning procedure is as follows (see Fig. 4). First, the extracted spectra are normalized and columns with < 20 per cent transmission are masked to remove the cores of saturated telluric lines, while 15 columns at both edges of each order which show enhanced systematics are additionally masked. Any remaining outliers on the scale of a single pixel are detected through application of a Laplacian of the Gaussian algorithm, or 'Blob Detection Algorithm' (e.g. Kong, Akakin & Sarma 2013, see van Sluijs et al. 2023), and pixels that deviate by $> 5\sigma$ are masked. Following this, the spectra are shifted into the stellar rest frame through flux conserving interpolation. For each night a master spectrum, containing stellar and telluric spectral features, is created using the mean of all spectra for each nodding position. Due to the low number of frames available per nodding position (\sim 25) and the 1:1 ratio of $T_{\rm in}$: $T_{\rm out}$ frames, we construct this master spectrum using all frames, not just the out-of-transit frames. Subsequently, each spectrum is divided by the master spectrum of the corresponding nodding position (Panel C; Fig. 4). As the planet spectral lines are Doppler-shifted by \sim 14 km s⁻¹ across the in-transit frames, the planetary signal is rapidly shifting between spectral pixels. Any self-subtraction of the planetary signal through the inclusion of the in-transit frames is therefore ≤ 4 per cent. Injection-recovery tests confirm that the higher precision master spectrum produced when using spectra from all exposures sufficiently negates any possible self-subtraction of the planet. Following the division by the master spectra columns with standard deviations $> 4\sigma$ are masked to remove high variance columns.

At this stage significant residuals still remain, which are removed through the application of the de-trending algorithm SYSREM (Tamuz,

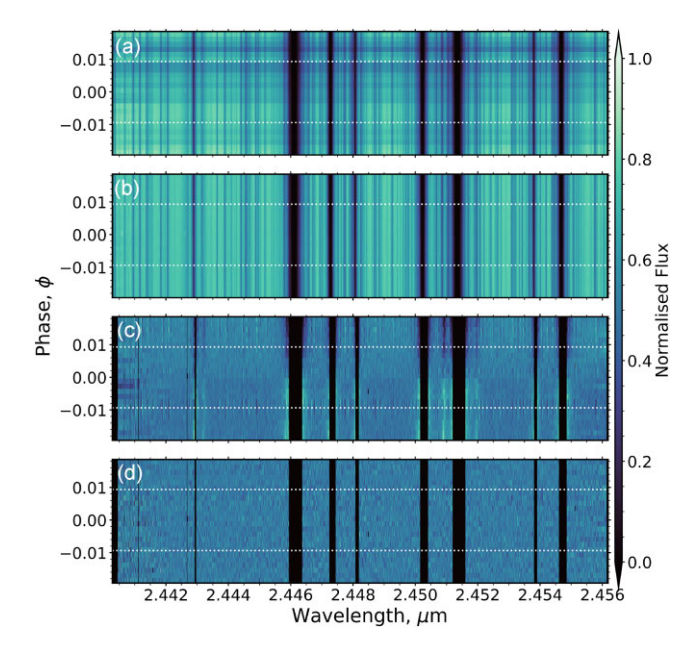


Figure 4. The data processing stages for the four CRIRES+ transits, with transit ingress and egress marked by the white dashed horizontal lines. Panel A shows the optimally extracted and phase ordered spectra, following basic calibrations including background subtraction. Panel B shows the normalized, wavelength calibrated spectra, where any residual large scale trends have been removed through division by a smoothed spectrum. Panel C shows the spectra shifted into the stellar rest frame, where saturated telluric lines and high variance columns have been masked following bad pixel correction and division by the master spectrum constructed from the mean of all exposures. Finally, Panel D shows the spectra after SYSREM is applied iteratively to remove remaining linear systematic trends in the data. These resulting cleaned spectra are subsequently cross-correlated with planetary models. This figure shows the B nod spectra extracted from the first order of the second detector during the second transit.

Mazeh & Zucker 2005; Mazeh, Tamuz & Zucker 2007; Birkby et al. 2013). SYSREM iteratively identifies and removes linear systematic trends from the data, incorporating the error of each data point. However, SYSREM requires the adoption of a robust stopping criteria to prevent erosion of the planetary signal, and to avoid the optimization of systematic noise. Here, we apply the data-driven approach of Spring & Birkby (in preparation), and calculate the $\Delta_{\mathcal{S}}$ metric for each iteration, defined as:

$$\Delta \varsigma = \frac{^{(i-1)}\sigma - ^{(i)}\sigma}{^{(i-1)}\sigma},\tag{1}$$

where ${}^{(i-1)}\sigma$ and ${}^{(i)}\sigma$ are the standard deviation of the data before and after the i-th iteration of SYSREM, respectively. This metric therefore encapsulates the percentage change in the standard deviation of the data for the application of each SYSREM iteration. The stopping point of SYSREM is selected to be the iteration at which $\Delta_{\mathcal{S}}$ plateaus, and is calculated independently for each detector order (See Fig. C1). The number of SYSREM components removed for each data set is displayed in Table A1.

3.3 Atmospheric models

3.3.1 Atmospheric models for cross-correlation

In order to extract the faint planet spectrum from the residual noise in the processed data, we need to combine the signal from each of the planetary spectral lines. We achieve this via cross-correlation with

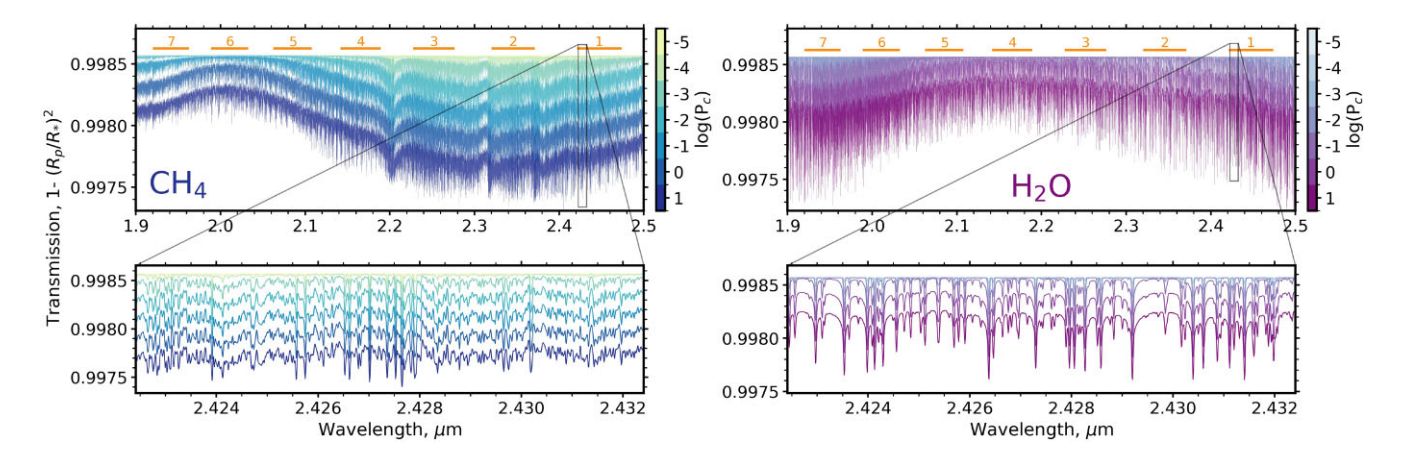


Figure 5. High spectral resolution models of GJ 3090 b with CH₄ (left) and H₂O (right) as the only spectroscopically active atmospheric constituents. The colour gradient delineates models with an aerosol layer at pressure level P_c in bar. A rising aerosol layer truncates spectral lines in the transmission spectrum, reducing their detectability, although this effect is less pronounced than at lower spectral resolution as the cores of the $R = 146\,000$ lines extend above the aerosol layer. For each model, P_0 is fixed to the cloud deck pressure. The wavelength regions covered by the CRIRES+ K2166 grating are highlighted in orange.

high-resolution model spectra derived from atmospheric models (Fig. 5). To generate the spectral templates, we calculate how the apparent size of the planet changes for a grid of atmospheric gases and cloud top levels.

For our transmission model templates, we have taken into account the contribution from the dominant and most readily detectable molecular species from the following line list data bases: CO2 (Rothman et al. 2010), CO (Li et al. 2015), CH₄ (Hargreaves et al. 2020), H₂O (Polyansky et al. 2018), H₂S (Azzam et al. 2016), and NH₃ (Coles, Yurchenko & Tennyson 2019). The absorption crosssections for each molecule at different pressures and temperatures were calculated using the open-source custom opacity calculator HELIOS-K (Grimm et al. 2021), where we assume Voigt line profiles for the absorption lines, 0.01 cm⁻¹ spectral resolution, and a constant line cutoff of 100 cm⁻¹. We have also taken into account the Rayleigh-scattering contribution from each molecular species and the collision-induced absorption (CIA) from H2-H2 and H2-He (Richard et al. 2012). The concentrations for each chemical species were calculated using the FastChem model (Stock et al. 2018). The atmospheric composition structure of GJ 3090 b is still poorly constrained observationally, and its values may depart from chemical equilibrium by processes such as atmospheric dynamics, condensation chemistry, and photochemistry (e.g. Venot et al. 2014; Mendonça et al. 2018b). However, due to the poor constraints on these processes, we adopt a simple prescription for the atmosphere probed by the transmission spectra, assuming chemical equilibrium, and an isothermal profile at the equilibrium temperature (a reasonable approximation given the S/N of the planetary spectrum, e.g. Young, Spring & Birkby 2024). Cloud decks in our models are represented by a layer of large particles that act as grey absorbers, providing a parametrization that is agnostic to the specific aerosol (cloud or haze) species that results in obscuration of the spectra. Our model calculates the transmission spectra with $R \sim 250\,000$ following the formalism presented in Gaidos, Kitzmann & Heng (2017), Bower et al. (2019), and Bello-Arufe et al. (2023), and the spectra are subsequently broadened to the measured instrumental resolution ($R \sim 146\,000$) prior to cross-correlation. The model computes the effective tangent height in an atmosphere discretized into 200 annuli. The code operates on GPUs and effectively generates a grid of atmospheric models for various metallicity levels and cloud tops used in this work. We note that, while GJ 3090 b has precise measurements of the planetary mass and radius (Almenara et al. 2022), the uncertainty on these parameters propagates into an uncertainty on the planetary scale height of 33 per cent.

3.3.2 Self-consistent atmospheric models

In Section 5, we compare the temperature profiles of two different scenarios in the atmosphere of GJ 3090 b to the saturation vapour pressure profiles of various cloud compositions. This is to evaluate the possible species that might condense in its atmosphere, and these models are not used for cross-correlation. The temperature profiles are calculated using the HELIOS model (Malik et al. 2017, 2019), and the gas concentrations are computed by the FastChem model (Stock et al. 2018), under the assumption of atmospheric chemical equilibrium. The HELIOS model employs k-distribution tables for opacities, integrating radiative fluxes over 383 spectral bands and 20 Gaussian points. Opacities are calculated using the HELIOS-K model (Grimm et al. 2021). We have included the main absorption species: H2O (Barber et al. 2006), CO2 (Rothman et al. 2010), CO (Li et al. 2015), CH₄ (Yurchenko & Tennyson 2014), NH₃ (Yurchenko, Barber & Tennyson 2011), HCN (Harris et al. 2006), PH₃ (Sousa-Silva et al. 2015), C₂H₂ (Gordon et al. 2017), H₂S (Azzam et al. 2016), Na and K (Burrows, Marley & Sharp 2000; Kurucz 2011). Additionally, we incorporate Rayleigh scattering cross-sections for H₂ and He (Lee & Kim 2004; Sneep & Ubachs 2005), and the CIA from H₂-H₂ and H₂-He (Richard et al. 2012).

The incoming stellar radiation in the model is represented by an interpolated PHOENIX model (Husser et al. 2013). HELIOS represents the atmospheric convection by mixing the enthalpy instantaneously in a buoyant unstable atmospheric region (Mendonça et al. 2018a; Malik et al. 2019), and the heat redistribution was set to 0.5, the default value for Sub-Neptune simulations with HELIOS (Malik et al. 2017). The model is integrated until the radiative-convective equilibrium criterium is achieved in every layer of the model.

3.4 Searching for planetary signals through cross-correlation

Following the removal of the stellar signal and telluric contamination, the residual spectra are primarily composed of noise, but additionally contain a contribution from the planetary spectrum, buried in the noise (Panel D; Fig. 4). To search for and extract this weak signal (S/N < 1 per line) we cross-correlate with model atmospheric spectra (see Section 3.3) through calculation of the Pearson correlation coefficient, ρ :

$$\rho_{X,Y} = \frac{C_{X,Y}}{\sqrt{C_{X,X} \cdot C_{Y,Y}}},\tag{2}$$

where $\rho_{X,Y}$ is the Pearson correlation coefficient between two matrices X and Y, and C is the covariance. A cross-correlation function (CCF) is produced for each model by calculating the correlation coefficient across systemic velocity shifts of ± 300 km s⁻¹, sampled at the CRIRES+ pixel velocity resolution of 1.5 km s⁻¹, and across orbital semi-amplitudes of ± 300 km s⁻¹. The planetary signal Doppler shifts by a velocity:

$$v_{\text{shift}} = v_{\text{bary}} + v_{\text{sys}} + K_{\text{p}} \sin(2\pi\phi_{\text{p}}), \tag{3}$$

where v_{bary} is the Earth's barycentric velocity offset, v_{sys} the systemic velocity of the host star relative to the Solar barycentre, $K_{\rm p}$ the semi-amplitude of the planetary orbit, and ϕ_p the orbital phase at the time of observation. For GJ 3090 b the systemic velocity is $v_{\rm sys}$ = 17.4095 ± 0.0046 km s⁻¹ (Almenara et al. 2022), and the orbital semi-amplitude is calculated to be $K_p = 121\pm1 \text{ km s}^{-1}$ under the assumption of a circular orbit. We subsequently construct K_p-v_{sys} maps for each transit and nodding position, alongside the map for the combined data set. When searching for molecular signals from the planetary atmosphere the individual CCFs from each order are combined using a weighted sum, in which we weight each map by the average observed S/N of the spectra used to construct it, and by the number of unmasked data points used in the calculation of the CCF. For each molecule we additionally exclude spectral orders containing no spectral features of the target molecule to prevent the additional inclusion of noise in the CCF. These maps are then used to search for molecular signatures in the planetary spectrum (Section 4), in which a signal is considered a detection if it is located at the specific systemic velocity (v_{sys}) and orbital semi-amplitude (K_p) of GJ 3090 b, and has a S/N > 5. The S/N is calculated by dividing each row in the $K_p - V_{sys}$ matrix by the standard deviation of that row. Systemic velocities within $\pm 20 \text{ km s}^{-1}$ of the planetary systemic velocity are excluded from the calculation of standard deviation to avoid the inclusion of potential planetary signals in the noise estimate.

3.5 Log-likelihood mapping for injection tests

The Pearson cross-correlation coefficient and the S/N detection metric are well suited for searching for planetary spectral features, due to the sensitivity to the location and depth of the spectral lines. However, in order to place statistically robust upper limits on the planet properties through injection tests (See Section 4.1), a more strict metric is required to determine the significance at which an injected model can be detected. We therefore adopt CCF to Loglikelihood mapping, developed for Bayesian parameter estimation (Brogi & Line 2019), which enables a statistical comparison between the respective fits of successive injected models. When calculating Likelihood values, we must now account for the fact that the planetary spectral lines in the data are modified by the cleaning process used (Brogi & Line 2019). Both the division of the master spectrum and the application on detrending algorithms (in this case SYSREM) modify and distort the relative depths of the planetary spectral lines (Gandhi et al. 2022; Gibson et al. 2022). We must therefore apply the same line distortions to the model templates used to cross-correlate with the data, in a process known as model reprocessing (Dash et al. 2024). The process adopted is as follows. When detrending

the data, we save the components removed by the division of the master spectrum and by each SYSREM iteration. Prior to each cross-correlation, we construct a noiseless matrix of the model to be cross-correlated, incorporating the specific systemic ($v_{\rm sys}$) and planetary ($K_{\rm p}$) velocities. This matrix is subsequently reprocessed through application of the saved components, such that the model template has undergone the same processing as the planetary spectra in the data. Following the reprocessing of the model templates, we calculate the log likelihood, log(L), following Brogi & Line (2019):

$$\log(L) = -\frac{N}{2}\log\left[s_f^2 - 2R(s) + s_g^2\right]$$
 (4)

in which s_f^2 is the variance of the data, s_g^2 the variance of the model, and R(S) the cross-covariance

$$s_f^2 = \frac{1}{N} \sum_{n} f^2(n)$$
 (5)

$$s_g^2 = \frac{1}{N} \sum_{n} g^2(n - s) \tag{6}$$

$$R(S) = \frac{1}{N} \sum_{n} f(n)g(n-s)$$
 (7)

which maps to the cross-correlation coefficient by

$$C(S) = \frac{R(s)}{\sqrt{s_f^2 s_g^2}} \tag{8}$$

equivalent to the Pearson coefficient ρ . Here the value f(n) represents the mean-subtracted values of a row from each order of the processed data, and g(n) the corresponding processed model template, where n is an individual spectral channel, s denotes a wavelength shift, and N is the total number of spectral pixels used in the calculation. We calculate $\log(L)$ values for each transit, order, and detector individually and these are co-added without additional weighting for each injection test, as the $\log(L)$ calculation accounts for the weighting of each section of the data. Following the calculation of the $\log(L)$ for each K_p – v_{sys} matrix, these are converted to confidence intervals using a likelihood ratio test (Pino et al. 2020). Following Lafarga et al. (2023) and Dash et al. (2024), the Likelihood ratio statistic (λ) is defined as

$$\lambda = 2[\log(L_{\text{max}}) - \log(L)] \tag{9}$$

in which $\log(L_{\max})$ is the maximum likelihood within the K_p – v_{sys} matrix, corresponding to the peak of the planet signal in the case of a strong detection. Following Wilks' theorem (Wilks 1938), the Likelihood ratio statistic follows a χ^2 distribution. As we explore two parameters, the systemic velocity of the host star (v_{sys}) and the semi-amplitude of the planetary orbit (K_p), this distribution has two degrees of freedom for each planetary model tested. The p-value of this χ^2 distribution is subsequently calculated, from which the confidence intervals are derived in units of standard deviation (σ). The model with the highest $\log(L)$, corresponding to the best fit to the data, therefore has $\sigma=0$, and models with increasingly poor fits to the data have increasing σ .

3.5.1 Metric for calculating the confidence at which an injected model can be excluded

In the case of non-detection, when seeking to place upper limits on the planetary properties, we require an additional metric to rule out groups of atmospheric models. To transform the λ metric into the confidence at which a model is excluded in an injection-recovery test

(see Section 4.1), we subtract the confidence value at the planetary position (denoting the best-fitting model in the case of a strong detection) from the mean confidence value of the matrix which encapsulates the 'noise' in the confidence map, excluding the ± 20 km s⁻¹ $v_{\rm sys}$ range surrounding the planetary systemic velocity. This $\Delta\sigma$ metric is thus a reformulation, in log(L), of the S/N metric commonly used with cross-correlation values in HRCCS (which simply compares the peak of the CCF for the detected planet signal to its standard deviation e.g. Brogi et al. 2014). Note that this metric differs from the log(L) metric used in injection-recovery grids shown in previous works as it provides an absolute detection significance for each recovered model, in comparison to the metric used in Lafarga et al. (2023) and Dash et al. (2024) which measures the quality of fit for each recovered model with comparison to the best-fitting recovered model.

4 RESULTS

We observe no robust detections (S/N > 5) of molecular species in the atmosphere of GJ 3090 b when using both the primary data set of four K2166 transits (10 h, excellent data quality), and upon the addition of the two K2148 transits (5.5 h, average-poor data quality). Principal challenges include the stellar and telluric contamination which reduce the achievable contrast limits on planetary spectral features (see Section 5.2), and can even produce convincing false positives. However, when injecting our planetary models into the data we see that we can recover signals at high S/N for a range of molecules (Fig. 6). In the absence of molecular detections we can therefore assess the sensitivity of our data using grids of injection-recovery tests to constrain the atmospheric properties of the planet (Section 4.1).

4.1 Injection tests

In the event of a non-detection of atmospheric features with HRCCS, injection tests have been widely used to constrain the atmospheric properties of the observed planet (e.g. Hoeijmakers, Snellen & van Terwisga 2018b; Merritt et al. 2020; Deibert et al. 2021; Spring et al. 2022; Lafarga et al. 2023; Dash et al. 2024; Grasser et al. 2024). We carry out injection tests for a grid of parameters for each molecule we aim to detect, with metallicities ranging from 1 to 1000 times solar metallicity ($Z = 1, 10, 100, 150, 200, 250, 500, 1000 \, Z_{\odot}$), and cloud top pressures spanning six orders of magnitude from 10^1 to 10^{-5} bar ($\log(P) = 1, 0, -1, -2, -3, -4, -5$ bar). The contribution functions of the planetary spectra (parametrized by the log opacity Jacobian; e.g. August et al. 2023) show sensitivity to atmospheric regions from $\sim 1-10^{-6}$ bar and thus the highest pressure cloud top tested, 10 bar, represents an effectively clear atmosphere scenario (see Fig. C2).

It is vital that the injected signals are subjected to identical processing as the real planetary signals and we inject model transmission spectra into the data immediately following spectral extraction and telluric wavelength calibration, but crucially prior to the removal of systematics. However, the impact of correlated noise and line distortions on the model spectra from instrumental effects cannot be accounted for, and therefore the injection tests will always be more sensitive to injected signals than planetary spectral features. Accordingly, we adopt strict 5σ upper limits when quoting constraints on planetary properties from our analysis.

Initially, we inject an atmospheric model containing a single molecular species, then cross-correlate with that same model. These simple injections demonstrate that HRCCS with CRIRES+ is theoretically sensitive not only to key molecules such as CH₄ and H₂O

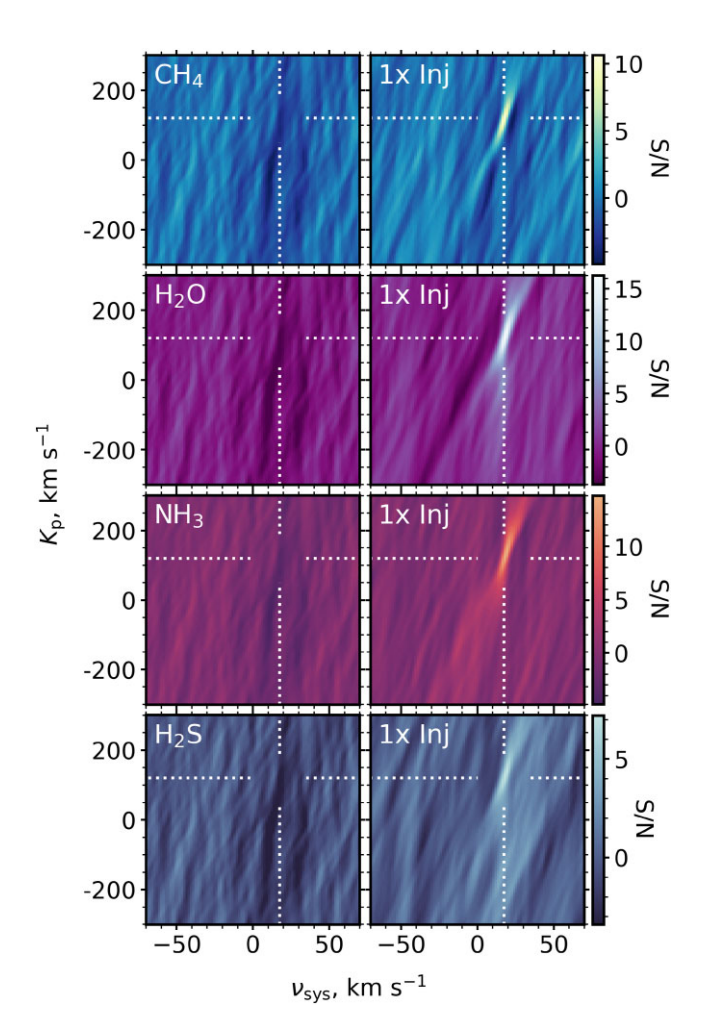


Figure 6. Left: the combined K_p – v_{sys} map from the four K2166 transits of GJ 3090 b for cross-correlation with CH₄, H₂O, NH₃, and H₂S templates (1 bar cloud deck, $10~\rm Z_{\odot}$ metallicity). No signals are observed at the expected planetary orbital and systemic velocities at sufficient significance to support a planetary origin. Note the anticorrelation at the planetary K_p , which is offset by \sim 5 km s⁻¹ from the planetary systemic velocity. This likely arises from the overlap of stellar and telluric residual noise when combining the four transits, but does not impact the recovery significance of injected models when using the log(L) mapping. Right: the recovery of the same models (1 bar cloud deck, $10~\rm Z_{\odot}$ metallicity) injected into the four transit data sets. Each of these models can be recovered at high S/N, demonstrating the constraining power of the data.

in sub-Neptune atmospheres, but also to trace molecular species including NH₃ and H₂S (e.g. Fig. 6). The atmospheric constraints produced from the single-species injection-recovery method are shown in Fig. C3. However, this method only provides a measure of the sensitivity of the data to a specific trace species in isolation. While this like-for-like approach may be appropriate for atmospheres dominated by a single trace species (e.g. Lafarga et al. 2023; Dash et al. 2024; Grasser et al. 2024), it is not necessarily accurate for more complex spectra where a multitude of molecular species can obscure the spectral lines from any individual molecule. This effect is particularly pronounced in the K-band, and injections of a single species model are at risk of overestimating the constraining power of the data. We therefore proceed to inject the data with a model containing opacities from all our considered species (i.e. CH₄, H₂O, NH₃, H₂S, CO₂, and CO) at their equilibrium abundances, but then cross-correlate with model templates containing only a

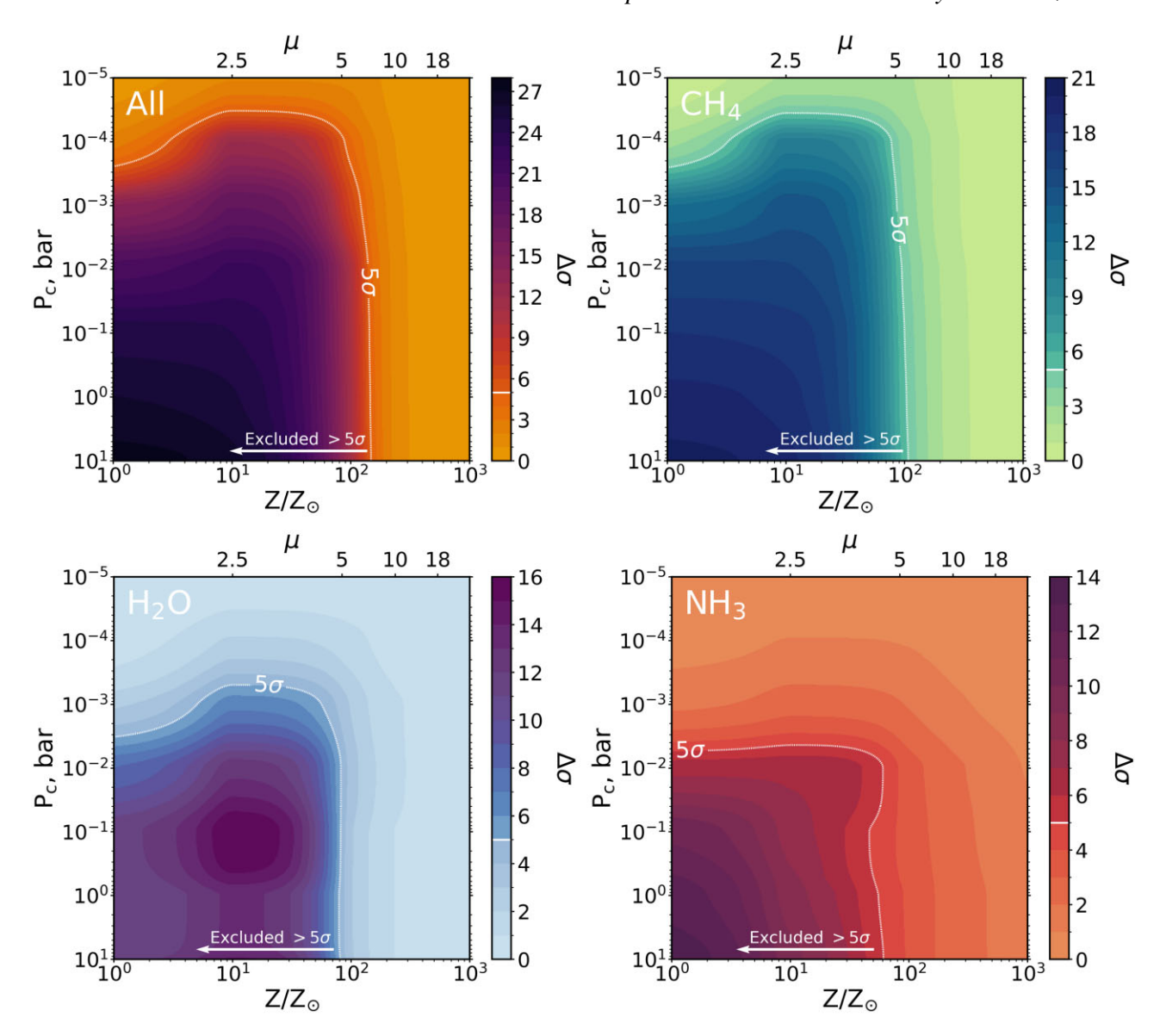


Figure 7. Recovered significance on the planetary signal ($\Delta\sigma$) when performing all-species injection-recovery tests, i.e. where a model containing spectral features from all considered molecules (CH₄, H₂O, NH₃, H₂S, CO₂, CO) is injected, and a template containing only a single molecule is used to recover it. The exception is the top left panel where the cross-correlation template matches the all-species injected model. Dark regions denote areas of the parameter space where the injected model is confidently recovered to > 5σ and thus ruled out as a plausible scenarios for the planetary atmosphere. The sensitivity of the data to CH₄ is largely invariant across the all versus single-species injection methods (see Fig. C3). Low metallicities with low cloud decks are strongly disfavoured. The molecules for which we have no constraining power in these injection-recovery tests are shown in Fig. C4.

single species. This process more faithfully reproduces the analysis procedure used in traditional HRCCS to detect genuine planetary signals, in which a model template containing spectral features from a single species is cross-correlated with the complex spectrum of the observed planet. Consequently, this all-species injection-recovery approach is more robust against the overestimation of atmospheric constraints, though it does inherently assume the choice of the injected all-species model is a good representation of the atmosphere of GJ 3090 b.

The results of these all-species injection-recovery tests are shown in Fig. 7. These injection tests demonstrate that the data are highly sensitive to a large range of atmospheric scenarios, across multiple molecular species, and demonstrate two overarching trends across the recovered models. First, increasing the atmospheric metallicity (Z), corresponding to an increase in the mean molecular weight (MMW,

 $\mu)$ of the atmosphere through the enrichment of heavier elements, drives a reduction in the atmospheric scale height. This mutes spectral features and results in poor detectability at high metallicity. For $\rm H_2O$ the largest spectral features are achieved for a $10\times$ solar metallicity atmosphere (10 $\rm Z_{\odot}$), as the increased abundances of the targeted molecular species, due to an enriched reservoir of oxygen in the atmosphere, outweighs the impact of the reduced scale height. All species show a sharp drop off in detectability for very high metallicity atmospheric scenarios $\gg 100~\rm Z_{\odot}$.

Second, the detectability of a model is reduced by cloud decks at increasingly high altitudes, due to the truncation of spectral lines in the transmission spectrum (Fig. 5). While the damping effect of high altitude aerosol layers is dominant at lower spectral resolution, at the resolving power of $R = 146\,000$ we see a much weaker dependence of detection significance on cloud top pressure, confirming predictions

for observations of cloudy sub-Neptunes with HRCCS (Gandhi et al. 2020; Hood et al. 2020). Counterintuitively, the models which can be excluded at highest significance for $\rm H_2O$ are at cloud deck pressures of $\rm 10^{-1}$ bar rather than at $\rm 10^{1}$ bar, the lowest altitude cloud pressure in the grid. We suggest that this behaviour arises as the $\rm H_2O$ features in the central CRIRES+ K2166 orders (orders 3 and 4), which additionally contain strong CH₄ spectral features, are suppressed for models with higher cloud decks, preventing obscuration of the lines in the $\rm H_2O$ model template by the CH₄ lines that dominate the injected model, and thus increasing the retrieved significance of the $\rm H_2O$ signal.

The injection tests also illustrate that the data is largely insensitive to the carbon bearing species CO and CO₂, even for low metallicity atmospheric scenarios with low altitude clouds (Fig. C4). For CO₂, this is largely due to the CO₂ features in the K-band falling in regions of contamination from telluric CO2. The lack of sensitivity to CO is impacted by the strong dependence of the CO lines on the cloud deck pressure and metallicity, and is complicated by strong stellar residuals from deep CO lines in the M-dwarf stellar spectrum, and the impact of the Rossiter-Mclaughlin effect (See Section 5.2.2). Uniquely, however, the CO₂ injections have marginal sensitivity to very high metallicity scenarios with $Z > 500 \, Z_{\odot}$. This is because a higher MMW drives an increasing CO2 abundance due to the enrichment of volatile carbon and oxygen, and thus produces larger spectral features in transmission, despite the decreasing scale height with metallicity. The CO₂ constraints from the single species model injections therefore weakly disfavour the highest metallicity scenarios for low altitude clouds at $\sim 3\sigma$.

The two atmospheric scenarios constrained by this data are degenerate. Using the injected model containing all planetary features, the injection-recovery tests indicate that GJ 3090 b has either a high metallicity (Z \gtrsim 150 Z_{\odot}), high mean molecular weight ($\mu > 7.1$) atmosphere (with an aerosol layer at pressures $\lesssim 10^{-2}$ bar), or an aerosol layer at pressures $< 3.3 \times 10^{-5}$ bar for which the metallicity is unconstrained.

4.2 Inclusion of archival CRIRES+ data

When carrying out the all-species injection-recovery using the full equilibrium chemistry models (Section 4.1), the archival K2148 transits are only sensitive to CH₄ and H₂O. The constraints placed on the atmospheric properties from these two transits alone are limited to the relatively modest 5σ constraints on the atmospheric metallicity, $Z>30~Z_{\odot}$, and mean molecular weight $\mu>3.9$ for cloud decks $>6\times 10^{-3}$ bar, and can only exclude cloud decks at a maximum pressure of $>3.3\times 10^{-3}$ bar, two orders of magnitude less constraining than the four K2166 transit constraints (see Fig. B1).

The addition of these two archival K2148 transits to the K2166 data set does not therefore offer any significant improvements on the atmospheric constraints. While their inclusion marginally increases the significance at which the most readily detectable (i.e. low metallicity, low altitude cloud deck) scenarios can be ruled out, it also provides a net decrease in the upper limits placed, due to the inclusion of additional noise in the CCFs for the more challenging atmospheric scenarios, for which these archival transits have no constraining power.

Under idealized photon-dominated Poisson statistics the constraints from 2 transits have 71 per cent of the sensitivity of 4 transits. However, the disparity in constraining power between the K2166 transits and the archival K2148 transits exceeds this, and is driven primarily by the difference in data quality, as a result of contrasting observing conditions. While the four transits in the K2166

grating are performed under excellent stable seeing conditions (Avg. FWHM of 0.5 arcsec), the two archival K2148 transits are observed in variable seeing conditions (see Table B1), with an average FWHM of 0.81 and 1.10 arcsec, respectively, impacting the stability and S/N of the spectra. The airmass at mid transit for the second archival K2148 transit additionally suffers from higher airmass pre-transit frames, reaching up to an airmass of 1.8. The S/N per exposure is consequently reduced, from an average of 155 for the four K2166 transits, to an average of 89 for the two archival transits, equivalent to a factor of 3 discrepancy in observing time under Poisson statistics.

Furthermore, due to the lower quality and variable seeing conditions, the MACAO system did not consistently suppress the stellar FWHM < 0.2 arcsec, the CRIRES+ slit width, during the archival K2148 transits of GJ 3090 b, resulting in a spectral resolution of $R \approx 92\,000$. In comparison, the first four transits of GJ 3090 b achieve FWHM < 0.2 arcsec, leading to super-resolution effects and spectral resolutions in excess of R = 140000 (See Section 3). As the S/N scaling for HRCCS increases with $\sqrt{N_{\text{lines}}}$ lines, this results in an additional theoretical increase in the S/N of 26 per cent when comparing observations taken with a spectral resolution of $R = 92\,000$ compared to $R = 146\,000$, due to the increase in the number of resolvable planetary spectral lines (when using the CH₄ models used in this work). A high spectral resolution is particularly valuable for HRCCS observations of hazy sub-Neptunes in transmission, as it allows for the cores of narrow spectral lines truncated by high altitude aerosol layers to be resolved. However, we caution that while the super-resolution is advantageous in this work, it introduces challenges to the data analysis, namely systematic differences between A and B nods and the potential for time varying systematics driven by slit losses if the narrow PSF is permitted to wander in the slit. If the increased spectral resolution exceeds the Nyquist sampling frequency of the detector in the dispersion direction, then the increased spectral resolution will offer diminishing returns due to undersampling of the extracted spectra.

Finally, the two K2148 observations additionally suffer from high and variable precipitable water vapour (PWV) across the transits, reaching maxima of 2.8 and 4.31 ppm. In the near-infrared H₂O is a key telluric molecule and the PWV impacts the strength of telluric contamination, while any variability imprints residual noise into the data following PCA-based cleaning (Chiavassa & Brogi 2019; Smith et al. 2024). Using the simple S/N scaling relation from Birkby (2018), we estimate that each individual transit of the four K2166 transits has approximately 2.2 times the sensitivity to the spectral features of GJ 3090 b than each of the archival K2148 transits.

5 DISCUSSION

5.1 The atmosphere of GJ 3090 b within the context of the sub-Neptune population

Henceforth, we adopt the constraints from the injection and recovery of the model containing all tested molecules ('All'; Fig. 7), which imply 5σ limits on the metallicity and MMW of $Z>150~Z_{\odot}$ and $\mu>7.1$ (for a cloud deck $\lesssim 10^{-2}$ bar), or an aerosol layer at pressures $<3.3\times 10^{-5}$ bar with the metallicity unconstrained. These results have similar constraining power on the atmospheric metallicity to previous studies of the warm-Neptunes GJ 436 b and GJ 3470 b using HRCCS (Dash et al. 2024; Grasser et al. 2024), but place constraints on the aerosol layers that are over an order of magnitude tighter. This is remarkable given that GJ 3090 b has approximately half the planetary radius of GJ 436 b and GJ 3470 b. While the scale height of GJ 3090 b assuming a H/He dominated atmosphere (H $_0=340~\rm km)$

is more favourable than GJ 3470 b ($H_0=335~\rm km$) and GJ 436 b ($H_0=210~\rm km$), when comparing the transmission spectroscopy metrics GJ 3090 b (TSM = 221) is a significantly more challenging target than GJ 436 b (TSM = 621) and GJ 3470 b (TSM = 354). These constraints are therefore testament to both the high quality data obtained with CRIRES+ and the wavelength coverage in the K-band, specifically the coverage of CH₄ spectral features, which provide the strongest constraints on cloud deck pressure.

A direct comparison of these CRIRES+ constraints to JWST results for GJ 3090 b is not yet possible (See Section 5.3). However, the sub-Neptunes TOI-836 c (Wallack et al. 2024) and TOI-776 c (Teske et al. 2025), both observed in transmission by JWST, provide an interesting comparison. The constraints on MMW and cloud deck pressure for GJ 3090 b placed by CRIRES+ are comparable to those placed on TOI-836 c and TOI-776 c, which required 6.8 and 14.6 h of JWST observing time, respectively. Both of these sub-Neptunes have similar radii to GJ 3090 b, but are more challenging targets for transmission spectroscopy due to higher masses and consequently reduced scale heights (TOI-836 c: $H_0 = 176$ km, TOI-776 c: $H_0 =$ 97 km, under the assumption of a H/He dominated atmosphere), and thus have reduced transmission spectroscopy metrics (TOI-836 c: TSM = 104, TOI-776 c: TSM = 44). None the less, the ability of CRIRES+ observations to place constraints on GJ 3090 b that are comparable to those that JWST is achieving for sub-Neptunes (albeit for more challenging targets) demonstrates the potential of HRCCS for the characterization of sub-Neptunes.

Furthermore, while we adopt the 5σ constraint in our analysis for robustness, we note that our 3σ constraints on cloud deck pressure on GJ 3090 b is similar to the 3σ constraint of 10^{-5} bar for low metallicity atmospheres on GJ 1214 b (TSM = 416), from 77 h of *HST* observations (Kreidberg et al. 2014). These CRIRES+ observations therefore demonstrate the significant constraining power of ground-based HRCCS on high altitude aerosol layers on hazy sub-Neptunes, requiring approximately one eighth of the observing time compared to *HST* to place equivalent constraints for a more challenging target.

However, the interpretation of the CRIRES+ constraints is hampered by the inherent degeneracy between high altitude aerosols truncating planetary spectral lines in transmission, and thus reducing the detectability of species; and increasing atmospheric metallicity, which shrinks the spectral features. One scenario consistent with these results is that the muted spectral features are driven by high altitude aerosols in a low metallicity ($Z < 100 \ Z_{\odot}$) atmosphere. Radiative-convective models of the vertical temperature structure of GJ 3090 b predict the formation of KCl, Na₂S, and ZnS condensates in equilibrium chemistry across a range of atmospheric metallicities (Fig. 8), with KCl and ZnS predicted to provide the key contributions to high altitude opacity.

The well studied warm sub-Neptune GJ 1214 b, observed to host both a high altitude haze layer and a metal rich atmosphere (Kreidberg et al. 2014; Gao et al. 2023; Kempton et al. 2023; Lavvas, Paraskevaidou & Arfaux 2024; Ohno et al. 2025; Schlawin et al. 2024), and with an equilibrium temperature $T_{\rm eq} = 596\pm19~\rm K$, provides a compelling comparison to GJ 3090 b ($T_{\rm eq} = 693\pm18~\rm K$), despite its ~2 times greater mass (8.17 \pm 0.43 $\rm M_{\bigoplus}$; Cloutier et al. 2021). Indeed the predicted condensates for GJ 3090 b mirror the predictions of KCl and ZnS condensates for GJ 1214 b (Morley et al. 2013; Kreidberg et al. 2014). For solar metallicity atmospheres for GJ 3090 b, ZnS condensates are predicted to be able to form at pressures ~ $10^{-4}~\rm bar$, sufficient to match the observed CRIRES+ constraints at solar metallicity. For atmospheres with increasing mean molecular weights the upper atmosphere cools, and the condensation curves for KCl, Na₂S, and ZnS shift to higher

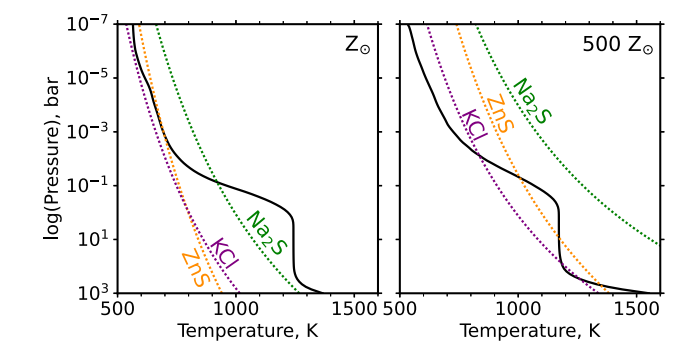


Figure 8. Model temperature-pressure profiles for a solar metallicity ($Z = Z_{\odot}$; left) and highly metal enriched atmosphere ($Z = 500 \ Z_{\odot}$; right) for GJ 3090 b, produced under radiative-convective equilibrium and for equilibrium chemistry using HELIOS and Fastchem (Malik et al. 2017; Stock et al. 2018; Malik et al. 2019), see Section 3.3. Condensation curves for key condensable species are plotted for each metallicity case, using the prescriptions from Morley et al. (2012) and Visscher, Lodders & Fegley (2006). For solar metallicity atmospheres ZnS condensates are predicted to be able to form at pressures $\sim 10^{-4}$ bar, sufficient to match the observed constraints.

temperatures, forming KCl and ZnS clouds at pressures $\sim 10^{-2}$ bar. To be the source of the non-detection, by causing truncated spectral features at high resolution, these condensates would therefore have to be transported to higher altitude regions of the atmosphere of GJ 3090 b, with pressures $< 10^{-4}$ bar. It has been suggested for GJ 1214 b that either vigorous internal mixing could loft condensates to higher altitudes (Charnay, Meadows & Leconte 2015a; Charnay et al. 2015b), or that mineral clouds of KCl and ZnS can rise to high altitudes if the cloud particles have sufficiently small radii, and thus have a low settling velocity (Morley et al. 2013, 2015). However, theoretical models have struggled to form sufficiently thick clouds at the required altitudes to match the flat transmission spectra of GJ 1214 b (Ohno & Okuzumi 2018; Adams et al. 2019).

An alternative scenario for aerosols on GJ 3090 b, proposed to explain the heavily dampened spectral features on GJ 1214 b, suggests a thick photochemical haze providing a strong opacity at NIR wavelengths (Kreidberg et al. 2014; Kempton et al. 2023). A wide range of species have been proposed as potential outcomes of haze formation in warm sub-Neptune atmospheres including tholins, hydrocarbon chains analogous to the haze on Saturn's moon Titan; complex molecules with chemical formulas $C_w H_x N_y O_z$; and diamonds formed through chemical vapour deposition (Gavilan et al. 2018; Hörst et al. 2018; Moran et al. 2020; Ohno 2024). The presence of a high altitude photochemical haze on GJ 3090 b would conform to and corroborate the growing evidence for the trend of haze production with temperature across the sub-Neptune population (Crossfield & Kreidberg 2017; Brande et al. 2024). Warm sub-Neptunes with 500 $< T_{\rm eq} < 800$ K have been identified to suffer from the greatest attenuation of spectral features, and GJ 3090 b, with an equilibrium temperature of 693±18 K, falls within this region of maximum attenuation.

However, the constraints placed in this work are also consistent with GJ 3090 b hosting a highly metal enriched envelope, with mean molecular weight $\mu > 7.1$ g mol⁻¹. A high metallicity scenario would be driven by a significant enrichment of CNOPS elements, forming increased molecular abundances of e.g. H₂O, CH₄, NH₃, and CO₂ and resulting in a declining mass fraction of H/He (Nixon et al. 2024). Addressing only the constraints on metallicity, the CRIRES+ observations appear consistent with a high metallicity

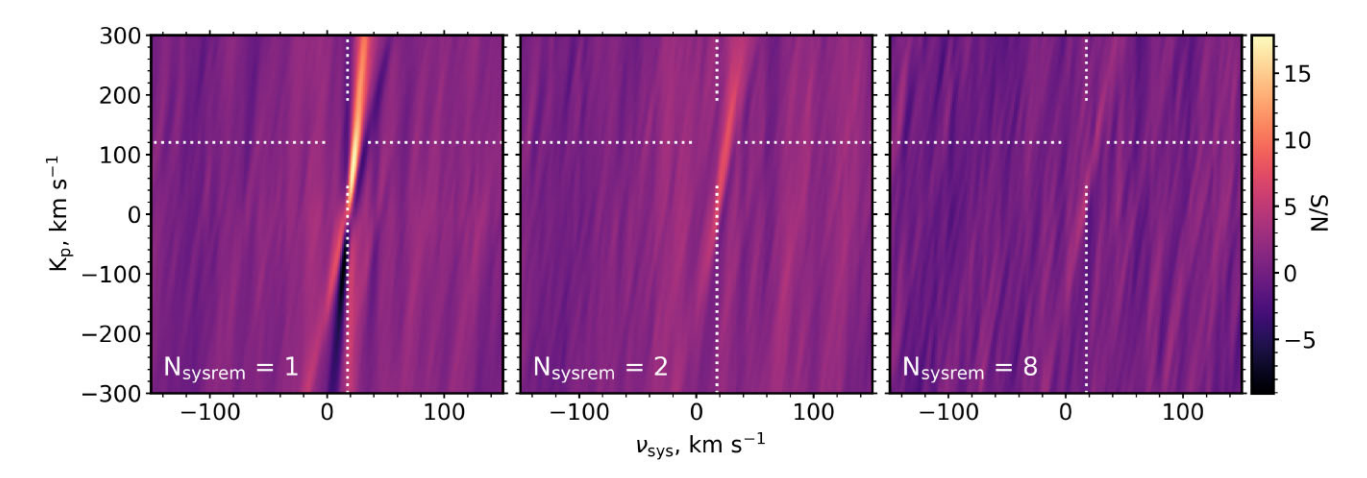


Figure 9. $K_p - v_{sys}$ maps resulting from the cross-correlation of the first night of CRIRES+ spectra with a PHOENIX stellar model template, demonstrating the evolution of residual M-dwarf features with increasing numbers of SYSREM components removed. The stellar residuals dominate following the removal of a single SYSREM component (left) with a distinctive asymmetric signal. Following the removal of two SYSREM components the stellar residual signal peaks at approximately the planetary K_p , masquerading as a redshifted planetary detection with S/N > 5 (centre). While eight SYSREM iterations are sufficient to reduce the stellar residuals to the average noise level of the $K_p - v_{sys}$ map (right), correlated noise still remains at the planetary position.

envelope composed of miscible H/He and metals (Benneke et al. 2024). Under the assumption of equilibrium chemistry and a solar C/O = 0.55, the CRIRES+ observations imply a metal mass fraction $Z_{\rm atm} > 67$ per cent for the low altitude cloud deck scenarios. This in turn provides an upper bound on the H/He envelope mass fraction of $x_{\rm H/He} < 33$ per cent, implying that GJ 3090 b is not H/He dominated if a high metallicity atmosphere drives the non-detections in this work. This estimate relies on the additional assumptions of a well mixed envelope in chemical equilibrium, with a He mass fraction Y = 0.275.

While this result is dependent upon the assumption of equilibrium chemistry and the adopted C/O ratio, it is largely insensitive to the exact chemical mixing ratios of the volatile species. These observations therefore disfavour a 'Gas Dwarf' composition for GJ 3090 b (Fortney et al. 2013; Lopez & Fortney 2014), in which the atmosphere is dominated by H/He, and has a low mean molecular weight < 3.3 (Benneke et al. 2024). In order for this scenario to exist on GJ 3090 b either photochemical haze or clouds are required to form at pressures $< 10^{-4}$ bar. The high metal mass fraction $Z_{atm} > 67$ per cent is consistent with a 'Metal-Rich Miscible Envelope sub-Neptune' proposed by Benneke et al. (2024), but also approaches the 75 per cent metal mass fraction proposed to mark the transition to 'high-volatile-metal-mass-fraction worlds'. These planets are typified by the 'steam world' GJ 9827 d, seen to host spectral features from H₂O and a measured MMW of 18 g mol⁻¹ (Piaulet-Ghorayeb et al. 2024), but could theoretically be dominated by any volatile molecular species.

While the degeneracy with high altitude aerosol layers prevents detailed conclusion on the exact composition of the atmosphere of GJ 3090 b, the ability to exclude $\mu < 7.1$ scenarios for cloud decks $> 10^{-2}$ bar, is consistent with a highly metal enriched atmospheric composition, and a 'water world' scenario for GJ 3090 b cannot be excluded. Recent *JWST* observations of GJ 1214 b have raised the possibility of extremely metal enriched envelopes, $Z > 1000 \ Z_{\odot}$ alongside high altitude haze (Lavvas et al. 2024; Ohno et al. 2025; Schlawin et al. 2024), and GJ 3090 b also appears to be consistent with a similar composition. A highly metal enriched atmosphere on GJ 3090 b would likewise be consistent with the empirical massmetallicity trend shown by the Solar System planets (Wakeford &

Dalba 2020). However, these results are markedly different to the clear, low-metallicity atmosphere of TOI-421 b (Davenport et al. 2025), which orbits a G-type host star. The suppression of haze formation on TOI-421 b compared to GJ 3090 b may arise due to the higher equilibrium temperature ($T_{\rm eq} = 920\pm24~{\rm K}$) which results in the depletion of CH₄, a key haze precursor molecule. The low MMW atmosphere of TOI-421 b suggests distinct atmospheric evolution pathways for sub-Neptunes around FGK stars compared to M-dwarfs, and further highlights the diversity of atmospheres within the sub-Neptune population.

At present, the degeneracy between high altitude clouds and metal enrichment of the atmosphere on GJ 3090 b prevent detailed conclusions on its atmospheric composition and interior structure. None the less, the growing population of characterized warm sub-Neptunes with similar masses, equilibrium temperatures, and stellar environments (e.g. GJ 1214 b, GJ 9827 d) provide an initial indication that both metal rich atmospheres and high altitude haze are common within this population.

5.2 HRCCS strategies for M-dwarf host stars

This study is one of only a few HRCCS analyses of planets transiting M-dwarf host stars to date, alongside Ridden-Harper et al. (2023), Cabot et al. (2024), Dash et al. (2024), and Grasser et al. (2024). The profusion of molecular lines in M-dwarf host stars create unique challenges for HRCCS, so we offer here recommendations for improvements in HRS observations and analysis methods.

5.2.1 Joint modelling of stellar and telluric contamination

The fundamental challenge when observing M-dwarf host stars with HRCCS is the existence of two contaminating signals, in two separate rest-frames, in the form of the spectral features from the star and the tellurics. Uncorrected stellar spectral features induce particularly localized signals in K_p – $v_{\rm sys}$ maps, and can produce false positive signals at the planetary K_p or increase the background noise. We show in Fig. 9 the result of cross-correlating the data with an M-dwarf spectrum at various stages of the SYSREM detrending. The

PHOENIX stellar models capture the key molecular absorption features from H_2O and CO in the M-dwarf photosphere and thus provide a trace of the impact of stellar contamination when performing cross-correlations. However, they are not sufficiently accurate to directly model the observed stellar spectrum.

In this study we mask and detrend the data without separating the blended stellar and telluric lines. However, previous works have successfully modelled and removed stellar or telluric components from the data. For telluric spectral features the spectral synthesis code MOLECFIT (Smette et al. 2015) has been successfully applied to high spectral resolution data, principally at visible wavelengths where H₂O dominates the telluric spectrum (e.g. Allart et al. 2017; Hoeijmakers et al. 2018a; Bello-Arufe et al. 2022). Its use has also been explored for more challenging applications in the near infrared (e.g. González Picos et al. 2024), where the telluric spectrum is denser, and requires the modelling of multiple telluric species (e.g. H₂O, CH₄, CO₂), including saturated telluric lines (Smette et al. 2015). However, the M-dwarf spectrum of GJ 3090 in the K-band is dominated by shallow H₂O lines across the entire wavelength range, and deep CO lines at the 2.3 µm band head. These lines blend with features from the tellurics, complicating the fitting of telluric lines with MOLECFIT, and additionally remove all remaining continuum, which is required as a baseline by MOLECFIT to provide an accurate fit to the telluric transmission. In order to minimize the contamination from the M-dwarf spectrum, we attempt to use selected regions of the spectra containing relatively isolated and unobscured telluric features to fit a telluric model. However, there are an insufficient number of these unobscured telluric features to capture the behaviour of the multiple telluric molecules that impact our K-band spectra to the required accuracy, and this approach yields inadequate fits to our

Previous works have also successfully fit stellar spectral features, although these have been largely limited to narrow spectral regions (e.g. the 2.32 μm ro-vibrational CO lines in solar-type stars; Brogi et al. 2016). The use of numerical 3D hydrodynamical simulations of stellar photospheres has also been explored, and demonstrated to be highly effective at removing the stellar contribution from G and K-type stars (Chiavassa & Brogi 2019; Flowers et al. 2019). However, to date, this approach has not been extended to M-dwarf host stars, and models of stellar photospheres face challenges accounting for the impact of magnetic fields, spot coverage, and activity on synthetic spectra (Allard et al. 2013).

One opportunity for HRCCS is to adapt existing codes commonly used in extreme precision radial velocity (EPRV) planet searches [e.g. YARARA (Cretignier et al. 2021); WOBBLE (Bedell et al. 2019); SOFF (Gilbertson et al. 2024)] to perform data-driven modelling of the stellar and telluric lines. These methods rely on repeat observations separated by large barycentric velocity shifts to disentangle stellar and telluric signals, suited to EPRV searches. While unfeasible for single transit observations, this analysis method could potentially be applied to multitransit HRCCS observations, in which the observations are designed such that the epochs in which the transits are observed are well separated in barycentric velocity. Alternative approaches involve the reconstruction of telluric transmission spectra from a previously observed library of telluric standards (Artigau et al. 2014b). Existing HRCCS pipelines are implementing these techniques to remove telluric features, including the APERO pipeline for SPIRou/CFHT and NIRPS (Artigau et al. 2014a; Pelletier et al. 2021; Boucher et al. 2023), and these methods offer a promising approach for removing telluric contamination from HRCCS observations with ELT instrumentation.

5.2.2 The impact of the Rossiter-Mclaughlin effect

Over the course of a planetary transit, the planet occults different regions of the stellar disc, obscuring a fraction of the emitted flux. Due to the stellar rotation a net redshift of the integrated stellar line profile will be observed as the planet crosses the approaching blueshifted stellar hemisphere, and correspondingly a net blueshift when the planet crosses the receding redshifted stellar hemisphere. The resulting distortion of the stellar spectral line is known as the Rossiter-Mclaughlin (RM) effect or Doppler shadow (Cegla et al. 2016; Triaud 2018). When using HRCCS to search for a chemical species that is present in both the stellar photosphere and the planetary atmosphere, the distortion from the RM effect will produce signals in the CCF with a non-zero radial velocity shift as a function of time $(K_{\rm RM})$, and can therefore obscure or mimic a planetary signal (Brogi et al. 2016). As an M2V dwarf, GJ 3090 is expected to contain H2O and CO within its photosphere (Veyette et al. 2016), and we therefore run diagnostic tests to assess the potential impact of the RM effect on our observations.

We forward model a time-series of stellar and planet spectra. considering the stellar rotation and planet orbital motion. The stellar disc is simulated by division into a grid of 500×500 cells. Each cell is then assigned a stellar spectrum, for which we use a PHOENIX model retrieved for the stellar parameters provided in Table 1. The stellar disc is homogeneous, but rotating with $v \sin i = 1.468$ km s⁻¹ (Almenara et al. 2022), in which the contribution from each cell is shifted according to its relative velocity. The planet, with size and coordinates defined by the properties of GJ 3090 b (Table 1) and zero obliquity, is then introduced in transit across the stellar disc. This is initially represented by an opaque core; to include the planetary atmosphere, we take the models described in Section 3.3.1 and resample the opacity from each transited stellar cell according to the R_p/R_* at each wavelength. We then integrate the stellar and planet contributions, at time-stamps to match those of the observations (Section 2).

The simulated spectra are subsequently interpolated onto the observed wavelength grid, masked, and divided by the mean spectrum, following the post-processing procedures applied to the real CRIRES+ data, and a single SYSREM component is removed. We cross-correlate the residual spectral time-series with the injected model; our results from a single transit are plotted in Fig. 10. The CH₄ CCF shows no in-transit contamination from the RM effect, as is predicted due to the absence of CH₄ in the stellar photosphere. H₂O, known to be present in the M-dwarf spectra, shows only mild contamination from the Doppler shadow, and the planetary signal is dominant. The RM effect therefore does not manifestly alter the results of our injection-recovery tests involving H₂O, or molecules such as CH₄ which are not contained within the stellar photosphere.

Finally, CO shows near-total obscuration of the planetary signal across the transit, with a complex cross-correlation structure composed of three parts; the planetary CO trail, uncorrected stellar residuals, and the RM effect Doppler shadow. The planetary signal is limited to ingress and egress, while interference with the Doppler shadow appears to remove all information contained within the midtransit frames. Uncorrected stellar residuals, which are constant in phase, remain at ingress and egress, preventing the unique identification of the remaining planetary signal. The introduction of photon noise to the simulated data at the level seen in our observations results in the complete obscuration of the planetary CO features in the CCF. We therefore suggest that the RM effect is partially responsible for the complete lack of sensitivity to CO in the injection-recovery tests.

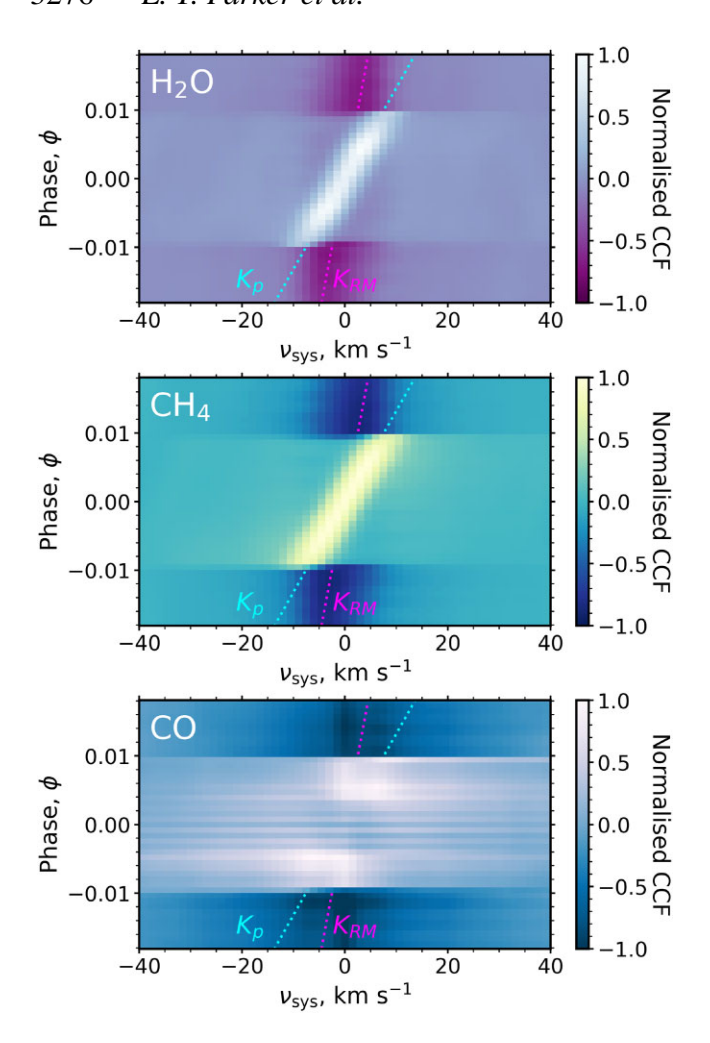


Figure 10. Noiseless simulations of the cross-correlation for GJ 3090 b transiting a rotating stellar disc, processed at the cadence of our observations. Both A and B nods are shown for clarity. Single species models containing $\rm H_2O$, $\rm CH_4$, and $\rm CO$ in a 10 $\rm Z_{\odot}$ metallicity atmosphere with a $\rm 10^1$ bar cloud deck are used for the planetary injection. The injected planetary signals of $\rm H_2O$ and $\rm CH_4$ appear largely unaffected by stellar contamination from the Rossiter-Mclaughlin effect, while the CO cross-correlation suffers from severe stellar contamination.

Due to the low velocity shift across the transit (\sim 14 km s⁻¹) the Doppler shadow and the planetary signal are coincident in velocity across the transit. Therefore established approaches of masking or modelling the Doppler shadow (e.g. Hoeijmakers et al. 2020; Prinoth et al. 2022; Maguire et al. 2023), risk removing or biasing the entirety of the planetary signal. It is therefore vital to consider the effect of the RM effect on target species when planning observations in the NIR around M-dwarfs, and to simulate the impact at the CCF level to ensure that the detection of atmospheric features is feasible.

5.2.3 Systemic velocity offsets

A vital consideration when planning transit HRCCS observations is to ensure that the systemic velocity of the target star relative to the solar barycentre (17.4095 km s⁻¹ for GJ 3090) is misaligned from the barycentric velocity of the Earth at the time of observation (Rodler & López-Morales 2014). For all HRCCS observations this is required to separate the planetary and telluric features in the $K_{\rm p}$ - $v_{\rm sys}$ parameter space, but the additional inclusion of strong stellar residuals from an

M-dwarf host creates a strong false positive risk from overlapping residuals if the systemic and barycentric velocities overlap. All of our nights have a velocity separation $> 5~\rm km~s^{-1}$ between the Earth's barycentric velocity offset and the stellar systemic velocity. However, we caution that 5 km s⁻¹ separation is the advisable limit for observations of M-dwarf hosts as the first transit of our data set, with an offset of 5.7 km s⁻¹, required additional attention while cleaning the data to avoid false positive planetary signals resulting from significant residuals from stellar and telluric overlap.

5.2.4 High resolution line lists in high MMW atmospheres

The accuracy of the line lists used in the generation of high-resolution model templates for cross-correlation is crucial for the successful detection of molecular species in exoplanet atmospheres (de Regt et al. 2022). As HRCCS progresses to the study of non-H/He dominated atmospheres, for example the $Z>100\ Z_{\odot}$ scenarios probed in this work (see Section 5), accurate spectral templates are required for the modelling of high mean molecular weight atmospheres. However, appropriate line broadening coefficients for non-H/He or non-telluric background gases are not readily available for the majority of atmospheric species of interest (Hedges & Madhusudhan 2016; Barton et al. 2017; Gharib-Nezhad & Line 2019; Vispoel, Fissiaux & Lepère 2019). With advances in HRCCS and the imminent advent of the ELTs, appropriate atmospheric templates are urgently required to facilitate the reliable and widespread use of HRCCS in high MMW atmospheres.

5.3 Predictions for JWST observations of GJ 3090 b

GJ 3090 b has been observed in transmission by *JWST*, as part of a programme to observe five potentially volatile-rich sub-Neptunes (ID.4098, PIs: Benneke, Evans-Soma; see Benneke et al. 2024; Piaulet-Ghorayeb et al. 2024; Ahrer et al., in preparation). Two transit observations were taken with NIRSpec using the G395H setting ($R \approx 2700$), and a further two transits observed with NIRISS single object slitless spectroscopy (SOSS; $R \approx 700$), providing spectral coverage from 0.6 to 5.27 μ m and totalling 20.82 h of observations. We simulate the detectability of specific planetary models tested in this work with the forthcoming *JWST* observations, using the *JWST* observation simulator PandExo (Batalha et al. 2017).

Two extreme atmospheric scenarios are presented in Fig. 11 that are not ruled out by the CRIRES+ observations. The first is a model with a metallicity of $1000\,Z_{\odot}$ and a low altitude 10 bar cloud deck, and the second an atmosphere with a high altitude aerosol layer at 10^{-5} bar and a solar metallicity. These idealized JWST simulations suggest that the upcoming observations have the theoretical sensitivity to detect molecular absorption features in transmission for high metallicity atmospheres, including CH₄ and H₂O features across the SOSS and G395H spectral ranges. Attenuation of the spectra by high altitude aerosols, under our modelling assumption of a grey cloud deck, has the largest impact in the SOSS spectral range and thus the SOSS data has the largest constraining power on cloud deck pressures at low resolution. The highest altitude aerosol layers tested ($<10^{-5}$ bar) completely obscure spectral features across the entire wavelength range (Fig. 11). For increasingly metal-enriched atmospheres, $> 1000 \, \mathrm{Z}_{\odot}$, CO₂ will dominate the atmospheric opacity, and may provide the most detectable signature of an extremely high metallicity atmosphere. While the 1.92-2.47 µm CRIRES+ observations presented in this work have limited sensitivity to CO₂ due to extreme telluric contamination and can only place $\sim 3\sigma$ constraints

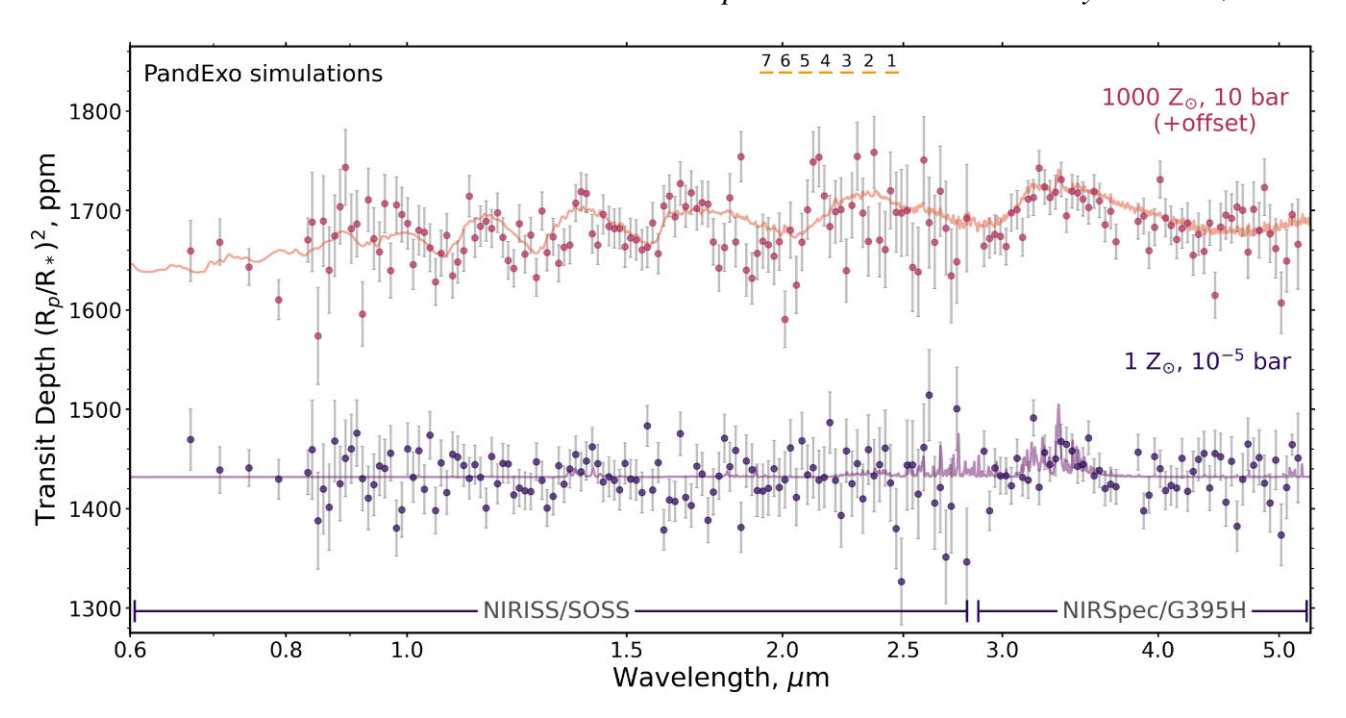


Figure 11. PandExo simulations of NIRSpec G395H (2 transits) and NIRISS/SOSS (2 transits) observations for atmospheric models for GJ 3090 b with a very high metallicity ($Z = 1000 \, Z_\odot$, 10 bar aerosol layer), and a very high altitude aerosol layer ($Z = 1 \, Z_\odot$, 10^{-5} bar aerosol layer), following the observing strategy of *JWST* programme ID.4098. The simulated models represent atmospheric scenarios which cannot be excluded by our high spectral resolution injection-recovery tests. The simulations do not include potential contamination from the M-dwarf host. *JWST* observations have sensitivity to the atmospheric metallicity through molecular features across the SOSS and G395H wavelength ranges, while high altitude grey aerosol layers obscure the spectral features in the SOSS wavelength range and return heavily muted features in the G395H spectra. The wavelength coverage of the CRIRES+ K2166 orders is denoted in yellow. The G395H and SOSS order 1 spectra are binned to R = 50, while SOSS order 2 is binned to R = 10.

on its presence, CO_2 is theoretically detectable in the NIRSpec G395H spectral range at 4.4 μm . With sufficient S/N from *JWST* the degeneracy between cloud deck pressure and atmospheric metallicity for GJ 3090 b could therefore be broken.

However, the impact of stellar contamination must also be considered. At a high spectral resolution the planetary atmosphere lines are resolved from the contaminating M-dwarf lines, due to their relative Doppler separation. At low spectral resolution these lines are blended and the presence of unocculted inhomogeneities (e.g. spots and faculae) in the photosphere of the M-dwarf host can directly contaminate the observed planetary transmission spectrum. This effect, known as the transit light source effect (TLSE; Rackham, Apai & Giampapa 2018) is wavelength-dependent and can result in spurious spectral signals, potentially orders of magnitude larger than planetary spectral features. While stellar contamination from the TLSE is principally a risk at the 0.6–2.8 μ m SOSS and 0.6–5.3 μ m NIRSpec Prism wavelengths (Lim et al. 2023; Cadieux et al. 2024; Radica et al. 2025), previous JWST studies of planets orbiting Mdwarfs have suffered from severe stellar contamination extending to 5 µm (e.g. May et al. 2023; Moran et al. 2023), preventing the unambiguous detection of species in the planetary atmospheres. However, we note that stellar contamination from the TLSE is not a universal issue for all M-dwarf hosts (e.g. Benneke et al. 2024), and that features from species that are not contained within the stellar photosphere (e.g. CH₄, CO₂), may still be detectable in the case of stellar contamination (e.g. Fournier-Tondreau et al. 2024).

HRCCS observations are highly complementary to low-resolution observations from *JWST*, as they probe distinct atmospheric pressures (Brogi & Line 2019), and joint retrievals of *JWST* and

ground-based high-resolution data present a promising avenue to provide tighter constraints on planetary properties (Smith et al. 2024). HRCCS can provide an independent probe of cloud deck pressures to break degeneracies in *JWST* data, as the 0.6–2.8 µm SOSS wavelengths, which provide the greatest sensitivity to aerosol layers with *JWST*, are at risk of stellar contamination from M-dwarfs. Furthermore, while *JWST* is theoretically sensitive to very high mean molecular weight atmospheres, in the case of a strongly obscured 0.6–2.8 µm SOSS spectrum (by either aerosol layers or stellar contamination), the MMW estimate can only be inferred from a single CH₄ or CO₂ feature in the NIRSpec G395H range, introducing considerable uncertainty (Benneke & Seager 2013; Benneke et al. 2024). HRCCS can therefore provide highly complementary MMW constraints which are less directly impacted by stellar contamination and high altitude aerosols.

5.4 Implications for future HRCCS studies of sub-Neptunes

GJ 3090 b is the sub-Neptune with the second highest TSM discovered to date (221^{+66}_{-46}) , and only GJ 1214 b is theoretically more readily observable in transmission. Through injection-recovery tests we have demonstrated that the CRIRES+ data are sensitive to a large range of atmospheric scenarios and thus low metallicity atmospheres with low altitude cloud decks on warm sub-Neptunes orbiting M-dwarfs can theoretically be observed using established HRCCS techniques. However, the non-detections presented in this work suggest that warm sub-Neptunes with high metallicity atmospheres and/or high-altitude aerosol layers remain beyond the observability of present instrumentation using only modest investments of observing

time. While we have demonstrated the sensitivity of HRCCS to the cores of spectral lines that extend above high altitude cloud decks (up to 3.3×10^{-5} bar in injection tests), the detection of spectral features from atmospheres with $Z \gg 150~\rm Z_{\odot}$ is currently prevented for any injected model by the reduced atmospheric scale height, resulting in muted spectral features. None the less, developments in stellar or telluric modelling, or novel detrending processes may offer some improvements in the sensitivity of HRCCS to these atmospheres (Section 5.2). Alternative avenues using existing HRCCS instrumentation could involve investigating sub-Neptune targets which have been predicted from population studies to have spectra less significantly attenuated by aerosols (e.g. $500 > T_{\rm eq} > 800~\rm K$; Crossfield & Kreidberg 2017; Brande et al. 2024).

The advent of the Extremely Large Telescopes (ELTs), will represent a step-change in the achievable S/N for the observation of exoplanetary atmospheres, nominally a factor of ~5 increase in the S/N on the planetary features based solely on scaling the primary mirror diameter from the VLT, and under the assumption of photon-dominated noise statistics. However, we caution that a myriad of instrumental parameters including, but not limited to, the wavelength coverage, relative throughput, instrument stability, achieved spectral resolution, and instrument specific systematic effects will all substantially impact the relative S/N achieved with ELT instrumentation (e.g. ANDES, METIS). Comprehensive end-to-end simulations, including all astrophysical and instrumental effects, are required to simulate HRCCS science cases for ELT instruments (e.g. Vaughan et al. 2024).

The S/N increase of the ELT alone will not guarantee the success of challenging observations, including those of hazy metal rich sub-Neptunes around M-dwarfs. Alongside the enduring observational challenges of telluric contamination, stellar residuals, and instrumental systematics; stellar effects including the RM effect, the transit light source effect, centre-to-limb variations, and stellar spectral variability over the observations will become increasingly prominent for observations with the sensitivity of the ELTs. These effects, while obscured at the present S/N, likely already inhibit our cleaning processes for GJ 3090 b (e.g. Section 5.2.2), and understanding their impact on HRCCS observations prior to observations with the ELT is vital.

Of particular promise for the study of warm sub-Neptunes with the ELTs are the *M*-band wavelengths (4–5 μm) covered by METIS/ELT (Brandl et al. 2021), and planned for GMTNIRS/GMT (Lee et al. 2022), and MICHI/TMT (Packham et al. 2018). This has been identified as the optimum spectral band for simultaneously detecting multiple species (CO, H₂O, CO₂, Haze species) in hazy sub-Neptunes in transmission (Hood et al. 2020), despite challenges from telluric contamination and thermal background, and the use of the *M*-band for HRCCS observations has recently been verified with CRIRES+ (Parker et al. 2024).

Moving beyond sub-Neptunes, the detection of molecular features in the atmospheres of rocky exoplanets around M-dwarf hosts using HRCCS in transmission is a key science goal for ELT instrumentation (e.g. ANDES/ELT; Palle et al. 2023). This challenging science case represents an order of magnitude increase in the sensitivity required on transit spectral features, from the scale heights to which we are sensitive to for GJ 3090 b (≥100 km), to scale heights of the order of 10 km expected for truly Earth-like exoplanetary atmospheres. The observations of challenging targets requires the stacking of cross-correlation functions from many transits, even with the ELTs (Currie, Meadows & Rasmussen 2023; Hardegree-Ullman et al. 2023). Given the risk of inducing false positives when performing this stacking, further work is required to fully explore the impact of combining

transits, and to identify diagnostics to delineate real and spurious signals (Cheverall & Madhusudhan 2024).

6 CONCLUSIONS

Using four CRIRES+ *K*-band (K2166) transits of the warm sub-Neptune GJ 3090 b we present the first dedicated search for molecular features in the atmosphere of a short period sub-Neptune using ground-based high-resolution spectroscopy. Despite achieving excellent data quality across all four transits we detect no molecular species. Through injection-recovery tests, we demonstrate the sensitivity of the data to CH₄, H₂O, NH₃, and H₂S, and verify the ability of HRCCS to access high aerosol layers on sub-Neptunes, placing constraints similar to those achieved with dedicated spacebased observatories (e.g. Kreidberg et al. 2014), in a fraction of the observing time. The inclusion of two archival CRIRES+ transits taken in the K2148 grating setting observed in more challenging observing conditions do not improve our constraints, demonstrating the importance of acquiring excellent quality data for this challenging science case.

The injection tests are consistent with two degenerate scenarios for the atmosphere of GJ 3090 b. First, GJ 3090 b may host a highly enriched atmosphere with $>150\,\rm Z_\odot$ and mean molecular weight $>7.1\,\rm g$ mol $^{-1}$, representing a volatile dominated envelope with a H/He mass fraction $x_{\rm H/He}<33$ per cent, with an unconstrained aerosol layer. Secondly, the data are consistent with a high altitude aerosol layer at pressures $<3.3\times10^{-5}$ bar, with the metallicity unconstrained. Cloud condensates are challenging to form at these altitudes on GJ 3090 b across a range of metallicities, and this attenuation by aerosols may therefore be driven by photochemical haze (Section 5). Comparing to the growing population of characterized sub-Neptune atmospheres in this temperature range, both metal enrichment and high altitude hazes remain viable scenarios within the warm sub-Neptune population.

Upcoming *JWST* observations of GJ 3090 b (ID.4098, PIs: Benneke, Evans-Soma) have the theoretical sensitivity to detect planetary spectral features in high metallicity atmospheres, and can therefore verify and extend the atmospheric constraints presented in this work. Through the access to high cloud decks HRCCS observations are highly complementary to low-resolution observations from *JWST*, and the combination of the unique sensitivities of the two methods has the potential to place powerful joint constraints on the atmospheric properties of GJ 3090 b.

Finally, we discuss the opportunities and challenges of observing the warm sub-Neptune population with both existing and future instrumentation for the ELTs. The M-dwarf host star poses specific challenges to the HRCCS analysis. Unlocking the full potential of the ELTs for atmospheric characterization will require significant improvements in the joint modelling and removal of telluric and M-dwarf spectral features, the calculation of molecular broadening coefficients for high mean molecular weight atmospheres, and a precise understanding of the impact of spectral variability from stellar inhomogeneities on high resolution spectra. Path finding studies using existing instrumentation to test ELT science cases are a crucial preparatory step to identify challenges prior to first light of the ELT.

ACKNOWLEDGEMENTS

We thank the referee for their helpful comments that improved the quality of the manuscript. We thank Eva-Maria Ahrer and Lisa Nortmann for helpful discussions. We additionally thank ESO astronomers Cedric Ledoux and Michael Abdul-Masih for taking the 109.232F observations and ensuring the excellent data quality which

has permitted this work. A special thank you to Ferdinando Patat in the ESO Observing Programmes Office for helping to make this observing programme possible.

LTP, JLB, SRV, and CF acknowledge funding from the European Research Council (ERC) under the European Union's Horizon 2020 research and innovation program under grant agreement No. 805445. JLB further acknowledges the support of the Leverhulme Trust via the Philip Leverhulme Physics Prize. JMM acknowledges support from the Horizon Europe Guarantee Fund, grant EP/Z00330X/1. A part of AB-A's contribution to this work was carried out at the Jet Propulsion Laboratory, California Institute of Technology, under a contract with the National Aeronautics and Space Administration (80NM0018D0004).

This study is based on observations collected at the European Organisation for Astronomical Research in the Southern Hemisphere under ESO programme 109.232F. This research has made use of the NASA Exoplanet Archive, which is operated by the California Institute of Technology, under contract with the National Aeronautics and Space Administration under the Exoplanet Exploration Program. This research has made use of NASA's Astrophysics Data System Bibliographic Services and the SIMBAD data base, operated at CDS, Strasbourg, France. This research made use of SAOImageDS9, a tool for data visualization supported by the Chandra X-ray Science Center (CXC) and the High Energy Astrophysics Science Archive Center (HEASARC) with support from the JWST Mission office at the Space Telescope Science Institute for 3D visualization (Joye & Mandel 2003). This work has made use of the Python programming language,³ in particular packages including NUMPY (Harris et al. 2020), SCIPY (Virtanen et al. 2020), MATPLOTLIB (Hunter 2007), and ASTROPY (Astropy Collaboration 2013, 2018, 2022).

DATA AVAILABILITY

The raw data used in this study is available for download from the ESO Data Archive under Programme IDs 109.232F and 0111.C-0106. Processed data products and models are available on reasonable request to the corresponding author.

REFERENCES

Adams D., Gao P., de Pater I., Morley C. V., 2019, ApJ, 874, 61

Aguichine A., Mousis O., Deleuil M., Marcq E., 2021, ApJ, 914, 84

Allard F., Homeier D., Freytag B., Schaffenberger W., Rajpurohit A. S., 2013, Mem. Soc. Astron. Ital. Suppl., 24, 128

Allart R., Lovis C., Pino L., Wyttenbach A., Ehrenreich D., Pepe F., 2017, A&A, 606, A144

Almenara J. M. et al., 2022, A&A, 665, A91

Artigau É. et al., 2014a, in Ramsay S. K., McLean I. S., Takami H., eds, Proc. SPIE Conf. Ser. Vol. 9147, Ground-based and Airborne Instrumentation for Astronomy V. SPIE, Bellingham, p. 914715

Artigau É. et al., 2014b, in Peck A. B., Benn C. R., Seaman R. L., eds, Proc. SPIE Conf. Ser. Vol. 9149, Observatory Operations: Strategies, Processes, and Systems V. SPIE, Bellingham, p. 914905

Astropy Collaboration 2013, A&A, 558, A33

Astropy Collaboration 2018, AJ, 156, 123

Astropy Collaboration 2022, ApJ, 935, 167

August P. C., Bean J. L., Zhang M., Lunine J., Xue Q., Line M., Smith P. C. B., 2023, ApJ, 953, L24

Azzam A. A. A., Tennyson J., Yurchenko S. N., Naumenko O. V., 2016, MNRAS, 460, 4063 Barber R. J., Tennyson J., Harris G. J., Tolchenov R. N., 2006, MNRAS, 368, 1087

Barton E. J., Hill C., Yurchenko S. N., Tennyson J., Dudaryonok A. S., Lavrentieva N. N., 2017, J. Quant. Spec. Radiat. Transfer, 187, 453

Basilicata M. et al., 2024, A&A, 686, A127

Batalha N. M., 2014, Proc. Natl. Acad. Sci., 111, 12647

Batalha N. E. et al., 2017, PASP, 129, 064501

 Bean J. L., Raymond S. N., Owen J. E., 2021, J. geophys. Res., 126, e06639
 Bedell M., Hogg D. W., Foreman-Mackey D., Montet B. T., Luger R., 2019, AJ, 158, 164

Bello-Arufe A., Buchhave L. A., Mendonça J. M., Tronsgaard R., Heng K., Jens Hoeijmakers H., Mayo A. W., 2022, A&A, 662, A51

Bello-Arufe A. et al., 2023, AJ, 166, 69

Benneke B., Seager S., 2013, ApJ, 778, 153

Benneke B. et al., 2019, ApJ, 887, L14

Benneke B. et al., 2024, preprint (arXiv:2403.03325)

Birkby J. L., 2018, preprint (arXiv:1806.04617)

Birkby J. L., de Kok R. J., Brogi M., de Mooij E. J. W., Schwarz H., Albrecht S., Snellen I. A. G., 2013, MNRAS, 436, L35

Boucher A. et al., 2023, MNRAS, 522, 5062

Bower D. J., Kitzmann D., Wolf A. S., Sanan P., Dorn C., Oza A. V., 2019, A&A, 631, A103

Brande J. et al., 2024, ApJ, 961, L23

Brandl B. et al., 2021, The Messenger, 182, 22

Brogi M., Line M. R., 2019, AJ, 157, 114

Brogi M., de Kok R. J., Birkby J. L., Schwarz H., Snellen I. A. G., 2014, A&A, 565, A124

Brogi M., de Kok R. J., Albrecht S., Snellen I. A. G., Birkby J. L., Schwarz H., 2016, ApJ, 817, 106

Buchhave L. A. et al., 2014, Nature, 509, 593

Burrows A., Marley M. S., Sharp C. M., 2000, ApJ, 531, 438

Cabot S. H. C., Madhusudhan N., Constantinou S., Valencia D., Vos J. M., Masseron T., Cheverall C. J., 2024, ApJL, 966, L10

Cadieux C. et al., 2024, ApJ, 970, L2

Cegla H. M., Lovis C., Bourrier V., Beeck B., Watson C. A., Pepe F., 2016, A&A, 588, A127

Charnay B., Meadows V., Leconte J., 2015a, ApJ, 813, 15

Charnay B., Meadows V., Misra A., Leconte J., Arney G., 2015b, ApJ, 813, L1

Cheverall C., Madhusudhan N., 2024, AJ, 167, 272

Chiavassa A., Brogi M., 2019, A&A, 631, A100

Cloutier R., Charbonneau D., Deming D., Bonfils X., Astudillo-Defru N., 2021, AJ, 162, 174

Coles P. A., Yurchenko S. N., Tennyson J., 2019, MNRAS, 490, 4638

Cretignier M., Dumusque X., Hara N. C., Pepe F., 2021, A&A, 653, A43

Crossfield I. J. M., Kreidberg L., 2017, AJ, 154, 261

Currie M. H., Meadows V. S., Rasmussen K. C., 2023, PSJ, 4, 83

Cutri R. M. et al., 2003, VizieR On-line Data Catalog: II/246. VizieR Online Data Catalog: 2MASS All-Sky Catalog of Point Sources (Cutri + 2003). Available at: https://ui.adsabs.harvard.edu/abs/2003yCat.2246....0C/abst ract

Dash S., Brogi M., Gandhi S., Lafarga M., Meech A., Bello-Arufe A., Wheatley P. J., 2024, MNRAS, 530, 3100

Dattilo A., Batalha N. M., 2024, AJ, 167, 288

Davenport B. et al., 2025, preprint (arXiv:2501.01498)

Deibert E. K., de Mooij E. J. W., Jayawardhana R., Ridden-Harper A., Sivanandam S., Karjalainen R., Karjalainen M., 2021, AJ, 161, 209

de Kok R. J., Birkby J., Brogi M., Schwarz H., Albrecht S., de Mooij E. J. W., Snellen I. A. G., 2014, A&A, 561, A150

de Regt S., Kesseli A. Y., Snellen I. A. G., Merritt S. R., Chubb K. L., 2022, A&A, 661, A109

Dorn R. J. et al., 2014, The Messenger, 156, 7

Dorn C., Venturini J., Khan A., Heng K., Alibert Y., Helled R., Rivoldini A., Benz W., 2017, A&A, 597, A37

Dorn R. J. et al., 2023, A&A, 671, A24

Esteves L. J., de Mooij E. J. W., Jayawardhana R., Watson C., de Kok R., 2017, AJ, 153, 268

³https://www.python.org/

Flowers E., Brogi M., Rauscher E., Kempton E. M. R., Chiavassa A., 2019, AJ, 157, 209

Fortney J. J., Mordasini C., Nettelmann N., Kempton E. M. R., Greene T. P., Zahnle K., 2013, ApJ, 775, 80

Fournier-Tondreau M. et al., 2024, MNRAS, 528, 3354

Fulton B. J., Petigura E. A., 2018, AJ, 156, 264

Fulton B. J. et al., 2017, AJ, 154, 109

Gaia Collaboration et al., 2021, A&A, 649, A1

Gaidos E., Kitzmann D., Heng K., 2017, MNRAS, 468, 3418

Gandhi S., Brogi M., Webb R. K., 2020, MNRAS, 498, 194

Gandhi S., Kesseli A., Snellen I., Brogi M., Wardenier J. P., Parmentier V., Welbanks L., Savel A. B., 2022, MNRAS, 515, 749

Gao P. et al., 2023, ApJ, 951, 96

Gavilan L., Carrasco N., Vrønning Hoffmann S., Jones N. C., Mason N. J., 2018, ApJ, 861, 110

Gharib-Nezhad E., Line M. R., 2019, ApJ, 872, 27

Gibson N. P., Nugroho S. K., Lothringer J., Maguire C., Sing D. K., 2022, MNRAS, 512, 4618

Gilbertson C. et al., 2024, preprint (arXiv:2408.17289)

González Picos D. et al., 2024, A&A, 689, A212

Gordon I. E. et al., 2017, J. Quant. Spec. Radiat. Transfer, 203, 3

Grasser N., Snellen I. A. G., Landman R., González Picos D., Gandhi S., 2024, A&A, 688, A191

Grimm S. L. et al., 2021, ApJS, 253, 30

Guo X. et al., 2020, AJ, 159, 239

Hardegree-Ullman K. K., Apai D., Bergsten G. J., Pascucci I., López-Morales M., 2023, AJ, 165, 267

Hargreaves R. J., Gordon I. E., Rey M., Nikitin A. V., Tyuterev V. G., Kochanov R. V., Rothman L. S., 2020, ApJS, 247, 55

Harris G. J., Tennyson J., Kaminsky B. M., Pavlenko Y. V., Jones H. R. A., 2006, MNRAS, 367, 400

Harris C. R. et al., 2020, Nature, 585, 357

Hedges C., Madhusudhan N., 2016, MNRAS, 458, 1427

Hoeijmakers H. J. et al., 2018a, Nature, 560, 453

Hoeijmakers H. J., Snellen I. A. G., van Terwisga S. E., 2018b, A&A, 610,

Hoeijmakers H. J. et al., 2020, A&A, 641, A123

Holmberg M., Madhusudhan N., 2024, A&A, 683, L2

Hood C. E. et al., 2020, AJ, 160, 198

Horne K., 1986, PASP, 98, 609

Hörst S. M., Yoon Y. H., Ugelow M. S., Parker A. H., Li R., de Gouw J. A., Tolbert M. A., 2018, Icarus, 301, 136

Hu R., Damiano M., Scheucher M., Kite E., Seager S., Rauer H., 2021, ApJ, 921, L8

Hunter J. D., 2007, Comput. Sci. Eng., 9, 90

Husser T. O., Wende-von Berg S., Dreizler S., Homeier D., Reiners A., Barman T., Hauschildt P. H., 2013, A&A, 553, A6

Jindal A. et al., 2020, AJ, 160, 101

Joye W. A., Mandel E., 2003, in Payne H. E., Jedrzejewski R. I., Hook R. N., eds, ASP Conf. Ser. Vol. 295, Astronomical Data Analysis Software and Systems XII. Astron. Soc. Pac., San Francisco, p. 489

Keles E. et al., 2022, MNRAS, 513, 1544

Kempton E. M. R., Perna R., Heng K., 2014, ApJ, 795, 24

Kempton E. M. R. et al., 2018, PASP, 130, 114401

Kempton E. M. R. et al., 2023, Nature, 620, 67

Kite E. S., Fegley B. J., Schaefer L., Ford E. B., 2020, ApJ, 891, 111

Kong H., Akakin H. C., Sarma S. E., 2013, IEEE Trans. Cybernet., 43, 1719

Kreidberg L. et al., 2014, Nature, 505, 69

Kurucz R. L., 2011, Can. J. Phys., 89, 417

Lafarga M. et al., 2023, MNRAS, 521, 1233

Landman R. et al., 2024, A&A, 682, A48

Lavvas P., Paraskevaidou S., Arfaux A., 2024, preprint (arXiv:2410.09981)

Lee H.-W., Kim H. I., 2004, MNRAS, 347, 802

Lee H. et al., 2022, in Evans C. J., Bryant J. J., Motohara K., eds, Proc. SPIE Conf. Ser. Vol. 12184, Ground-based and Airborne Instrumentation for Astronomy IX. SPIE, Bellingham, p. 121843I

Li G., Gordon I. E., Rothman L. S., Tan Y., Hu S.-M., Kassi S., Campargue A., Medvedev E. S., 2015, ApJS, 216, 15

Lim O. et al., 2023, ApJ, 955, L22

Lopez E. D., Fortney J. J., 2014, ApJ, 792, 1

Luque R., Pallé E., 2022, Science, 377, 1211

Madhusudhan N., Piette A. A. A., Constantinou S., 2021, ApJ, 918, 1

Madhusudhan N., Sarkar S., Constantinou S., Holmberg M., Piette A. A. A., Moses J. I., 2023, ApJ, 956, L13

Maguire C., Gibson N. P., Nugroho S. K., Ramkumar S., Fortune M., Merritt S. R., de Mooij E., 2023, MNRAS, 519, 1030

Malik M. et al., 2017, AJ, 153, 56

Malik M., Kitzmann D., Mendonça J. a. M., Grimm S. L., Marleau G.-D., Linder E. F., Tsai S.-M., Heng K., 2019, AJ, 157, 170

May E. M. et al., 2023, ApJ, 959, L9

Mazeh T., Tamuz O., Zucker S., 2007, in Afonso C., Weldrake D., Henning T., eds, ASP Conf. Ser. Vol. 366, Transiting Extrapolar Planets Workshop. Astron. Soc. Pac., San Francisco, p. 119

Mendonça J. M., Malik M., Demory B.-O., Heng K., 2018a, AJ, 155, 150 Mendonça J. M., Tsai S.-M., Malik M., Grimm S. L., Heng K., 2018b, ApJ, 869, 107

Merritt S. R. et al., 2020, A&A, 636, A117

Mikal-Evans T. et al., 2021, AJ, 161, 18

Mikal-Evans T. et al., 2023, AJ, 165, 84

Misener W., Schlichting H. E., Young E. D., 2023, MNRAS, 524, 981

Moran S. E. et al., 2020, PSJ, 1, 17

Moran S. E. et al., 2023, ApJ, 948, L11

Morley C. V., Fortney J. J., Marley M. S., Visscher C., Saumon D., Leggett S. K., 2012, ApJ, 756, 172

Morley C. V., Fortney J. J., Kempton E. M. R., Marley M. S., Visscher C., Zahnle K., 2013, ApJ, 775, 33

Morley C. V., Fortney J. J., Marley M. S., Zahnle K., Line M., Kempton E., Lewis N., Cahoy K., 2015, ApJ, 815, 110

Mousis O., Deleuil M., Aguichine A., Marcq E., Naar J., Aguirre L. A., Brugger B., Gonçalves T., 2020, ApJ, 896, L22

Nixon M. C., Madhusudhan N., 2021, MNRAS, 505, 3414

Nixon M. C. et al., 2024, ApJL, 970, L28

Nortmann L. et al., 2025, A&A, 693, A213

Ohno K., 2024, ApJ, 977, 188

Ohno K., Okuzumi S., 2018, ApJ, 859, 34

Ohno K. et al., 2025, ApJL, 979, L7

Packham C. et al., 2018, in Evans C. J., Simard L., Takami H., eds, Proc. SPIE Conf. Ser. Vol. 10702, Ground-based and Airborne Instrumentation for Astronomy VII. SPIE, Bellingham, p. 10702A0

Palle E. et al., 2023, preprint (arXiv:2311.17075)

Palle E. et al., 2025, preprint (arXiv:2502.19932)

Parc L., Bouchy F., Venturini J., Dorn C., Helled R., 2024, A&A, 688, A59 Parker L. T. et al., 2024, MNRAS, 531, 2356

Paufique J. et al., 2004, in Bonaccini Calia D., Ellerbroek B. L., Ragazzoni R., eds, Proc. SPIE Conf. Ser. Vol. 5490, Advancements in Adaptive Optics. SPIE, Bellingham, p. 216

Pelletier S. et al., 2021, AJ, 162, 73

Pelletier S. et al., 2023, Nature, 619, 491

Piaulet-Ghorayeb C. et al., 2024, ApJ, 974, L10

Piaulet C. et al., 2023, Nat. Astron., 7, 206

Pierrehumbert R. T., 2023, ApJ, 944, 20

Pino L. et al., 2018, A&A, 619, A3

Pino L. et al., 2020, ApJ, 894, L27

Polyansky O. L., Kyuberis A. A., Zobov N. F., Tennyson J., Yurchenko S. N., Lodi L., 2018, MNRAS, 480, 2597

Prinoth B. et al., 2022, Nat. Astron., 6, 449

Rackham B. V., Apai D., Giampapa M. S., 2018, ApJ, 853, 122

Radica M. et al., 2025, ApJL, 979, L5

Richard C. et al., 2012, J. Quant. Spec. Radiat. Transfer, 113, 1276

Ridden-Harper A. R. et al., 2016, A&A, 593, A129

Ridden-Harper A. et al., 2023, AJ, 165, 170

Rodler F., López-Morales M., 2014, ApJ, 781, 54

Rogers L. A., 2015, ApJ, 801, 41

Rogers L. A., Seager S., 2010, ApJ, 716, 1208

Rothman L. S. et al., 2010, J. Quant. Spec. Radiat. Transfer, 111, 2139

Roy P.-A. et al., 2023, ApJ, 954, L52

Schlawin E. et al., 2024, ApJL, 974, L33

Schlichting H. E., Young E. D., 2022, PSJ, 3, 127

Seo C., Ito Y., Fujii Y., 2024, ApJ, 975, 14

Shorttle O., Jordan S., Nicholls H., Lichtenberg T., Bower D. J., 2024, ApJ, 962, L8

Smette A. et al., 2015, A&A, 576, A77

Smith P. C. B. et al., 2024, AJ, 167, 110

Sneep M., Ubachs W., 2005, J. Quant. Spec. Radiat. Transfer, 92, 293

Snellen I. A. G., de Kok R. J., de Mooij E. J. W., Albrecht S., 2010, Nature, 465, 1049

Sousa-Silva C., Al-Refaie A. F., Tennyson J., Yurchenko S. N., 2015, MNRAS, 446, 2337

Spring E. F. et al., 2022, A&A, 659, A121

Stock J. W., Kitzmann D., Patzer A. B. C., Sedlmayr E., 2018, MNRAS, 479, 865

Stolker T., Landman R., 2023, Astrophysics Source Code Library, record ascl:2307.040

Tamuz O., Mazeh T., Zucker S., 2005, MNRAS, 356, 1466

Teske J. et al., 2025, preprint (arXiv:2502.20501)

Triaud A. H. M. J., 2018, in Deeg H. J., Belmonte J. A., eds, Handbook of Exoplanets. Springer, Cham, p. 2

Van Eylen V., Agentoft C., Lundkvist M. S., Kjeldsen H., Owen J. E., Fulton B. J., Petigura E., Snellen I., 2018, MNRAS, 479, 4786

van Sluijs L. et al., 2023, MNRAS, 522, 2145

Vaughan S. R. et al., 2024, MNRAS, 528, 3509

Venot O., Agúndez M., Selsis F., Tessenyi M., Iro N., 2014, A&A, 562, A51

Veyette M. J., Muirhead P. S., Mann A. W., Allard F., 2016, ApJ, 828, 95

Virtanen P. et al., 2020, Nat. Methods, 17, 261

Vispoel B., Fissiaux L., Lepère M., 2019, J. Mol. Spectrosc., 360, 1

Visscher C., Lodders K., Fegley B. J., 2006, ApJ, 648, 1181

Wakeford H. R., Dalba P. A., 2020, Phil. Trans. R. Soc. London Ser. A, 378, 20200054

Wallack N. L. et al., 2024, AJ, 168, 77

Wilks S. S., 1938, Ann. Math. Stat., 9, 60

Yang J., Hu R., 2024, ApJL, 971, L48

Young M. E., Spring E. F., Birkby J. L., 2024, MNRAS, 530, 4356

Yu X., Moses J. I., Fortney J. J., Zhang X., 2021, ApJ, 914, 38

Yurchenko S. N., Tennyson J., 2014, MNRAS, 440, 1649

Yurchenko S. N., Barber R. J., Tennyson J., 2011, MNRAS, 413, 1828

Zilinskas M., Miguel Y., van Buchem C. P. A., Snellen I. A. G., 2023, A&A, 671, A138

Table A1. The number of SYSREM components removed for each order (O1-7) and transit. Transits one to four, observed in the K2166 grating setting, form our primary data set while the K2148 transits form the archival data set.

	Grating	O1	O2	О3	O4	O5	O6	O7
Transit 1	K2166	8	9	7	7	7	7	10
Transit 2	K2166	9	9	10	9	7	6	7
Transit 3	K2166	9	8	7	8	8	9	6
Transit 4	K2166	8	9	10	7	7	9	10
Transit 5	K2148	10	10	10	8	9	10	-
Transit 6	K2148	5	8	8	5	8	5	-

APPENDIX A: CRIRES+ REDUCTION DETAILS

In the raw CRIRES+ K2166 frames we observe systematic vertical stripes in the detectors and assess that these features are likely readout artefacts. The CRIRES+ detectors contain a region at the base of the detector array which is baffled to prevent its exposure to light, and we therefore subtract the median of this region to calibrate out these artefacts. This is set by the --subtract_nolight_rows = True command in the esorex background subtraction and spectral extraction routines. We additionally find that the subtraction of a columnby-column fit to the pixel values between each order aids this calibration, and therefore set --subtract_interorder_column = True during the background subtraction stage. In spectral extraction we find a poor performance of the cosmic ray detection algorithm for this data set, and therefore apply a custom bad pixel detection routine following extraction (see the main text, Section 4). When extracting individual spectra we set the extraction oversampling to 13, and the swath width to 600 pixels, determined through testing to provide clean extraction and to remove both extraction artefacts on the order of individual pixels seen for lower extraction oversampling, and discontinuities in the continuum observed for lower swath widths.

APPENDIX B: DETAILS OF THE ARCHIVAL K2148 TRANSITS

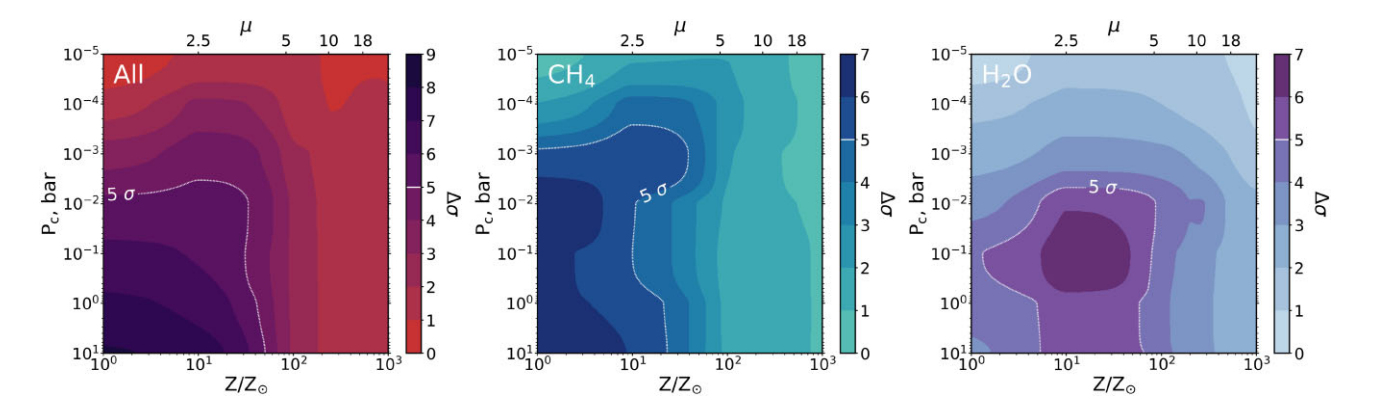


Figure B1. Same as Fig. 7 for the all-species injection recovery tests, but for the two archival K2148 transits. The archival transits place 5σ constraints on the model with full equilibrium chemistry (labelled All), and for CH₄ and H₂O, but not for any other considered species. Overall, the archival K2148 transits are two orders of magnitude less constraining on the pressure of the aerosol layer than the constraints from the four K2166 transits.

3282 L. T. Parker et al.

Table B1. Details of the archival 1.97–2.45 μm K2148 CRIRES+ observations of GJ 3090 b, denoted as Transit 5 and Transit 6.

	Transit 5	Transit 6		
UTC Date	11/08/2023	03/09/2023		
Avg. PWV	2.14 mm	4.10 mm		
Avg. Seeing	0.81 arcsec	1.10 arcsec		
Avg. Airmass	1.10	1.41		
N_{exp}	58	52		
DIT	180 s	180 s		
Slit Width	0.2 arcsec	0.2 arcsec		
Resolution	~92 000	\sim 92 000		
v_{bary} at T_0	$10.94 \; \rm km \; s^{-1}$	$4.48 \; km \; s^{-1}$		

APPENDIX C: ADDITIONAL FIGURES

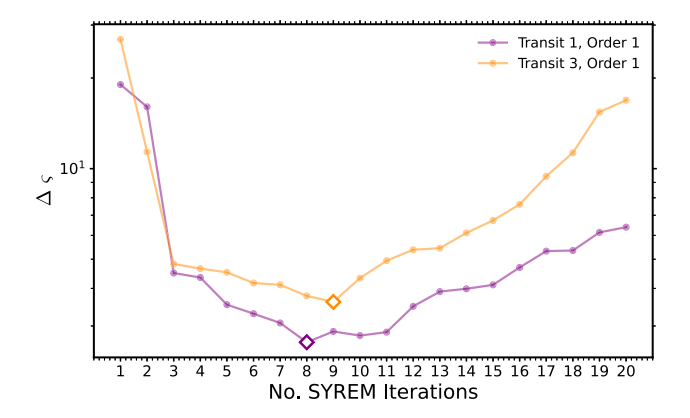


Figure C1. An example of the method used to determine the number of SYSREM components to remove from each order following the criteria of Spring & Birkby (in preparation), see Section 3.2.

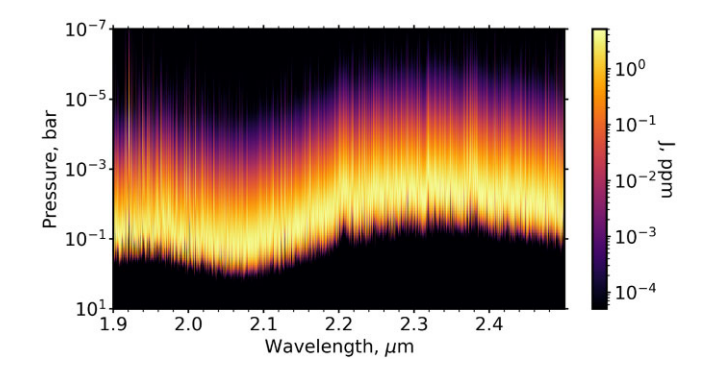


Figure C2. The log opacity Jacobian (J), demonstrating the atmospheric regions of GJ 3090 b probed by the model with solar metallicity, a 10 bar aerosol layer, and equilibrium chemistry.

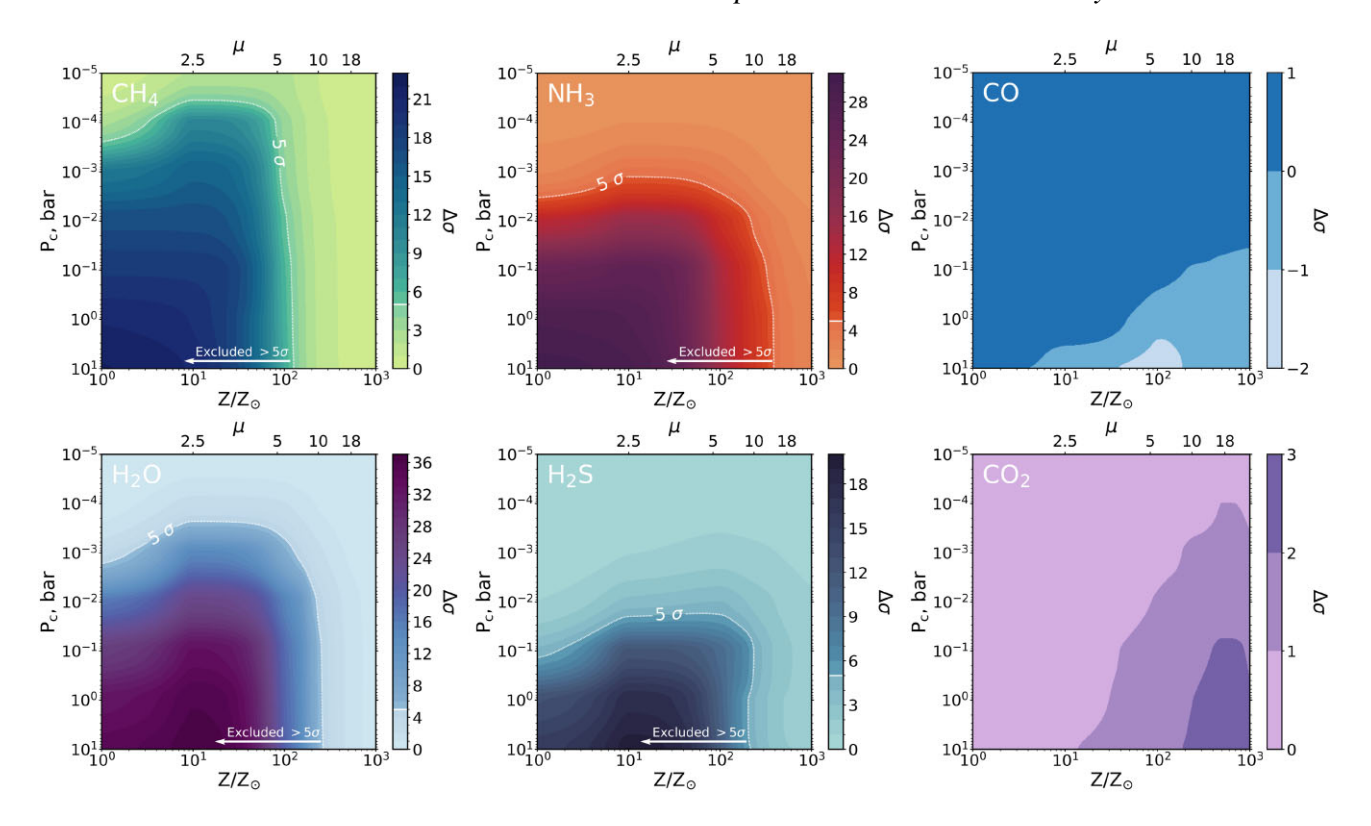


Figure C3. Recovered significance of the planetary signal ($\Delta\sigma$) when performing single-species injection-recovery tests across a grid of metallicities and cloud deck pressures, for CH₄, H₂O, H₂S, NH₃, CO, and CO₂. Dark regions denote areas of the parameter space where the injected model is confidently recovered to $> 5\sigma$ and would thus be ruled out as a plausible scenarios for the planetary atmosphere. Negative values of $\Delta\sigma$ denote that the recovered signal at the planet position is disfavoured compared to the measurement of the noise. We caution that single-species injection-recovery tests are at risk of overconstraining the planetary atmosphere due to the absence of obfuscating spectral features from other molecules.

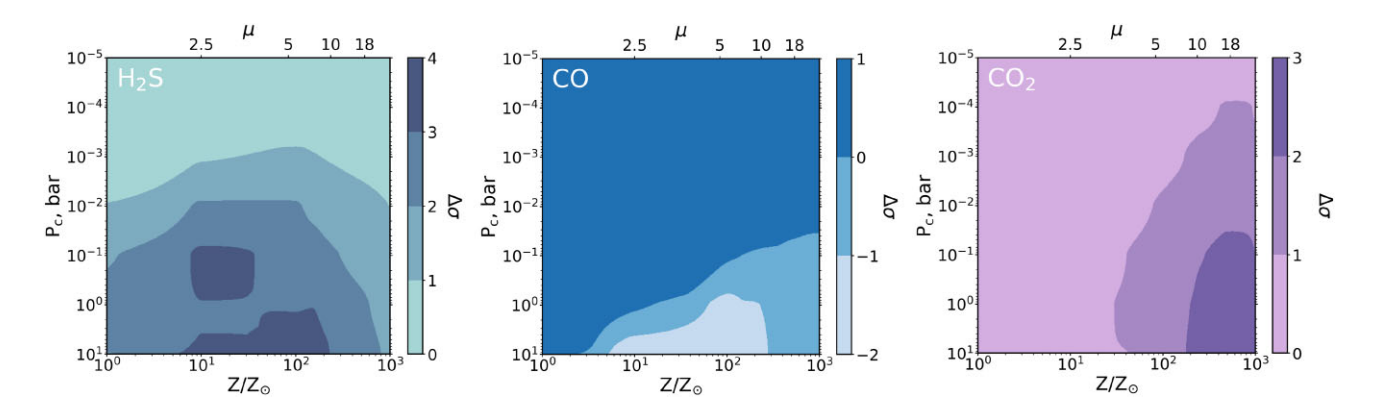


Figure C4. Same as Fig. 7 for the all-species injection-recovery tests, showing model templates with no significant constraining power (H_2S , CO, and CO_2). Negative values of $\Delta\sigma$ denote that the recovered signal at the planet position is disfavoured compared to the measurement of the noise.

This paper has been typeset from a TeX/IATeX file prepared by the author.